Application of redox sensitive proxies and carbonate clumped isotopes to Mesozoic and Palaeozoic radiaxial fibrous calcite cements

Ann-Christine Ritter [a,*], Tobias Kluge [b], Jasper Berndt [c], Detlev K. Richter [a], Cédric M. John [d], Stéphane Bodin [a], Adrian Immenhauser [a]

*Corresponding author: ann-christine.ritter@rub.de

[a] Ruhr-University Bochum, Institute for Geology, Mineralogy and Geophysics, Universitätsstraße 150, D-44801 Bochum, Germany

[b] Ruprecht-Karls-University Heidelberg, Institute of Environmental Physics, Im Neuenheimer Feld 229, D-69120 Heidelberg, Germany

[c] Westfalian Wilhelms University, Institute for Mineralogy, Corrensstraße 24, D-48149 Münster, Germany

[d] Department of Earth Science and Engineering and Qatar Carbonate and Carbon Storage Research Centre (QCCSRC), Imperial College London, Prince Consort Road, London SW7 2AZ, UK

Keywords

Carbonate, Diagenesis, Radiaxial fibrous calcite, Clumped isotopes, Rare earth elements

ABSTRACT

Ancient marine radiaxial calcite cements are commonly exploited as archives of marine porewater properties based on the argument that they lack metabolic effects often assigned to biogenic carbonates. Here we critically test the significance of conventional versus (with respect to these fabrics) less-conventional proxy data from Pennsylvanian, Triassic, and Cretaceous case examples. Conventional proxies include: cathodoluminescence, carbon and oxygen isotope ratios, main and trace elemental concentrations. Less conventionally applied proxies are: clumped isotope "Δ_{47}", redox-sensitive, and rare earth elements sampled across a succession of Triassic radiaxial fibrous calcites. Radiaxial calcites are subdivided in three groups based on their luminescence characteristics: non-luminescent, patchy luminescent, and bright luminescent. Luminescence patterns are in fair agreement with isotope ratios, in particular with those of oxygen. The data fall into, or are close, to the range of reconstructed marine seawater values and often plot to the positive end member of the isotopic range. These results disagree with the commonly held view that isotope data from luminescent cements reflect a priori non-marine values. Further evidence for this comes from REE concentration patterns and cerium-anomalies suggesting normal marine porewater values for all except the very last generation of radiaxial calcites. This implies that luminescent radiaxial calcites must not necessarily represent significant diagenetic resetting. Kinetic effects during precipitation and different activator elements must be considered. Marine and earliest burial porewater temperatures of ~12-26°C are suggested by conventional calcite $\delta^{18}O$ thermometry. Conversely, the application of the clumped isotope thermometer to the same radiaxial calcites suggests temperatures of 180-200°C, reflecting solid-state resetting of fully cemented limestones under a low water:rock ratio. Redox-sensitive elements, particularly Zn, Cd, U, and Cu are affected by kinetic processes overriding fluid Eh. Manganese concentrations and Ce-anomaly data point to gradually decreasing marine porewater oxygen levels from outer to inner cement fringes. Judging from REE patterns and Ce-anomalies, the cement layers in the central portions of the pore filling cement succession witnessed the end of marine precipitation and the onset of shallow marine diagenesis. Consequently, radiaxial calcite precipitation is suggested to continue in the early shallow (marine) burial domain. This study underscores the potential of radiaxial calcite successions as archives of

marine porewater to shallow burial diagenetic pathways. The combination of conventional and less conventional proxies is a clear strength of this study and documents that abiogenic carbonate archives are often underexplored.

1. Introduction

Radiaxial fibrous (RFC) and fascicular optical fibrous (FOFC) calcites (Bathurst, 1959; Kendall and Tucker, 1971; Kendall and Tucker, 1973; Kendall, 1976; Mazzullo et al., 1990; Swart, 2015) represent very common (up to 70 vol.-%) pore-filling cements in mainly Palaeozoic and Mesozoic marine carbonate buildups. Palaeogene and Neogene case examples of this marine carbonate fabric are remarkably scarce or perhaps even absent in the rock record (Aissaoui, 1988; van der Kooij et al., 2010). Although it is widely accepted that radiaxial fibrous calcite is an abiogenic precipitate (Richter et al., 2011), other authors, e.g., Lees and Miller (1995) discuss a microbial origin of similar cements but did not find evidence for this themselves.

In many cases, the presence of several stratigraphically overlying fringes of radiaxial and fascicular optical fibrous calcites occluding pore space in reefal carbonates represents a time-resolved archive of fluid properties recording gradual changes from the marine to increasingly burial domains. The common view is that these fabrics represent early marine diagenetic stabilization products of a high-Mg radiaxial fibrous calcite precursor phase whereas the controls that lead to the formation of their converging or diverging crystal c-axes axes are as yet unclear (see review in Richter et al., 2011). Assuming that marine porewater properties represent reasonable analogues of coeval marine waters, numerous workers have exploited there archives (Saller, 1986; Carpenter and Lohmann, 1989; Gray and Adams, 1995; Tobin et al., 1996; Kaufmann and Wendt, 2000; Kim and Lee, 2003; Hasiuk and Lohmann, 2008).

Most previous studies dealing with Palaeozoic or Mesozoic radiaxial fibrous calcites apply standard cathodoluminescence microscopy and conventional stable isotope ($\delta^{13}C$ and $\delta^{18}O$) combined with major and trace elemental (Mg, Mn, Sr, Fe) geochemistry in order to assess the nature and degree of diagenetic

overprint (Carpenter and Lohmann, 1989; Mazzullo et al., 1990; Bruhn et al., 1995; van der Kooij et al., 2007; 2009; Hasiuk and Lohmann, 2008). The commonly held opinion is that non-luminescence (black to blue intrinsic) typifies well-preserved material, whilst patchy or bright luminescent (radiaxial) calcites are considered as diagenetically altered and hence not applicable for the reconstruction of past seawater properties (see discussion in van der Kooij et al., 2007; 2009). Only a very limited number of workers exploited these fabrics in a more systematic manner as archives of their diagenetic pathways (e.g., Mazzullo et al., 1990; Kaufmann, 1997). Along these lines, Rare Earth Element (REE) data have the potential to shed light on the nature and properties of pore fluids and their evolution with time (e.g., German and Elderfield, 1990; German et al., 1991; Bodin et al., 2013; Della Porta et al., 2015) but have, to the knowledge of the authors, not yet been applied to these fabrics. The same accounts for the clumped isotopes (Δ_{47}) proxy revealing important information on burial fluid temperatures (e.g., Bernasconi et al., 2011; Huntington et al., 2011; Budd et al., 2013; Huntington and Lechler, 2015; Kluge et al., 2015; Shenton et al., 2015). Acknowledging that the REE proxy is a widely applied tool in geochemistry, we argue that its application to the fabrics studied here is rarely seen. The same accounts for redox sensitive elements and carbonate clumped isotope data. Therefore, referring specifically to radiaxial fibrous calcites, the label "less conventional" for the application of these proxies seems appropriate. The goal is to test if pore fluids from which some of these fabrics precipitated or stabilized might have properties that differed from that of coeval seawater.

The aims of this study are twofold: First, we document a comparison of geochemical and cathodoluminescence features of Pennsylvanian, Triassic and Cretaceous case examples of pore-filling successions of marine radiaxial calcites. Second, a particularly extensive succession of Upper Triassic radiaxial fibrous calcites was selected as a case example for an in-depth study of the diagenetic pathway recorded in these fabrics. In addition to conventional light stable isotopes and main and trace elements, we here also document clumped isotope, redox sensitive elements, and REE data from a transect across all paragenetic phases of these cements. This is performed with the intention to go beyond previously discussed

interpretations of these cement archives and to test the sensitivity of isotopic and elemental proxies for patterns and threshold limits in the diagenetic realm.

2. Description of case settings, sample materials and rationale for the selection of study sites

Below we briefly document the main characteristics of three Palaeozoic and Mesozoic case settings investigated here and refer to Table 1 for a summary of the main characteristics of the chosen time slices. The selection of sampling sites has been guided by the need for reasonably well dated, volumetrically significant, stratigraphically thick radiaxial fibrous cement successions in a shallow marine environment. A detailed framework of environmental and diagenetic parameters for all sampling sites exists. Most of the data (about 60%) shown here were obtained from Upper Triassic (Carnian to Norian; *ca* 227 -209 Ma) fibrous cements of Hydra Island (Greece). These are particularly suitable for this study due to their uncommonly thick cement fringes (~ 5 to 10cm). Approximately 20% of the samples studied originate from Pennsylvanian (Bashkirian; *ca* 323 - 311 Ma) of Northern Spain and approximately 20% from the Late Cretaceous (Cenomanian; *ca* 99 - 93 Ma) of Dokos Island (Greece; Table 1). Combining these three sample sets allows for deducing conclusions that go beyond that of a single case study.

2.1 Pennsylvanian of Asturias

The carbonate platform sampled in the context of this study, the Sierra del Cuera mountain range, is situated in the province of Asturias, Northern Spain (Fig. 1). This area forms part of the Cantabrian Zone characterized by a wide marine foreland basin during early Pennsylvanian time (Serpukhovian, 328-318 Ma). Nucleation of an extensive carbonate platform took place during Bashkirian (318-312 Ma) and Moscovian times (312-307 Ma; Colmenero et al., 2002; Bahamonde et al., 2007; van der Kooij et al., 2009). Due to tectonic rotation, outcrops of a high-rising margin of the platform are presently exposed in near-vertical position. The Bashkirian part of the margin, the Valdeteja Formation, has a progradational character

while the Moscovian portions (Picos de Europa Formation) are of aggradational nature (Bahamonde et al., 1997; Della Porta et al., 2004; van der Kooij et al., 2009). The Bashkirian upper-slope sequence, the sampling site of radiaxial calcites analysed in this study, is characterized by intercalated microbial boundstones, platform-shed grainstones and red-stained limestones with abundant successions of radiaxial fibrous calcites (Fig. 2A). These red intervals in the platform slope represent deepening pulses (van der Kooij et al., 2007).

2.2 Triassic of Hydra

The Greek island of Hydra is located offshore the Argolis Peninsula (Fig. 1). Hydra Island extends 18 km in EW and 4 km in NS direction (64.4 km²) and forms part of the Subpelagonian Zone, a passive continental margin succession belonging to the Internal Hellenides and has a transitional position to the Pindos zone (Jacobshagen, 1986; Richter, 1999). The geology of Hydra is characterized by three Tethyan neritic carbonate to siliceous hemipelagic successions trusted tectonically on top of each other. The oldest unit (I) is Permian in age and comprises large mud mounds embedded in their surrounding host sedimentary rocks. The stratigraphically overlying unit (II) is mainly characterized by Anisian (Middle Triassic) Tubiphyte reefal facies. The third unit (III) comprises sedimentary rocks of Upper Triassic (Carnian to Rhaetian) age and holds the tectonically uppermost position. It is mainly built by sponge-, coral- and algae-reefal facies (Richter, 1999). Sample locations for radiaxial fibrous calcites are mainly in the porous reefal texture of Unit IIIs reefal limestone facies (Fig 2B).

2.3 Cretaceous of Dokos

The island of Dokos (~15 km²) is located between Hydra Island and the mainland of Greece (Fig. 1). Dokos is mainly built by grey to dark red Cenomanian (Upper Cretaceous) bedded, neritic Akros limestones yielding abundant orbitolinid foraminifera and rudist bivalve remains (Clift and Robertson, 1990; Clift, 1996; Richter, 1999). Generally, the bedding of exposed units is thinning stratigraphically upwards and the

limestones represent an outer platform to slope setting. In northern Dokos, exposures of a stratigraphically thick, coarse breccia interval are exposed (Römermann, 1969). Pore spaces in these breccia bodies are often occluded by rims of radiaxial calcite cements sampled in the context of this study (Fig. 2C).

3. Definitions and terminology

Radiaxial fibrous (RFC) and fascicular optical fibrous (FOFC) carbonate fabrics (e.g., Kendall and Tucker, 1971; Kendall and Tucker, 1973; Kendall, 1976; Mazzullo et al., 1990) are composed of elongated (magnesian) calcite and rarely of dolomite (RFD; Hood and Wallace, 2012; Richter et al., 2014). These calcite cements show a characteristically distinct undulous extinction pattern when examined under crossed polarized light in a polarization microscope (Bathurst, 1959). Both fabrics reveal sub-crystals and a cloudy zonation and may include micro-inclusions (Davies and Nassichuk, 1990). Sub-crystals can either be identified by a displacement of the curvature of cleavage inside one crystal or by an unconformity in the movement of undulosity through the crystal. Radiaxial fibrous calcite fabrics, which are usually much more common relative to fascicular optical fibrous ones, are characterized by convergent c-axes while fascicular optical fibrous calcites reveal divergent c-axes (Fig. 3; Kendall, 1985). Furthermore, RFC fabrics display a characteristic upward concave curvature of cleavage, whilst the opposite is found for FOFC (Fig. 3; e.g. Kendall and Tucker, 1971; Kendall and Tucker, 1973; Mazzullo, 1980; Richter et al., 2011). Marine radiaxial calcites whereas such of shallow burial origin display increasingly planar cleavage. Following Richter et al. (2011), here the catch-it-all term “radiaxial calcite” is used for radiaxial fibrous and fascicular optical fibrous calcite unless specified differently. The finding of mainly radiaxial fibrous fabrics in Cretaceous belemnite guards (Richter et al., 2011) questions the strictly abiogenic nature of these particular cements. Radiaxial fibrous and fascicular optical fibrous calcite cements are not limited to marine environments but also common fabrics in vadose-meteoric cave depositional environments where they

include Holocene and present-day calcitic speleothems and flowstones (Richter et al., 2011), rimstones (Richter et al., 2015), or cryocalcites (Richter and Riechelmann, 2008).

4. Methodology

4.1. Microscopy

A total of ten thin sections from Pennsylvanian, Upper Triassic and Upper Cretaceous specimens (Fig. 2) have been analysed in detail by means of polarization and cathodoluminescence microscopy. Thin sections (2 x 3.6 cm) were used to characterize different fabrics under normal and polarized light. Cathodoluminescence (CL) microscopy has been applied in order to characterize zones of different CL characteristics using a HC1-LM hot cathode cathodoluminescence microscope developed at the Ruhr-University Bochum (Neuser et al., 1995). The electron beam is accelerated with 14 keV and the beam current is 0.2 mA. Rather than documenting spatially limited portions of thin sections by cathodoluminescence, a total of 120 to 150 individual CL images per thin section were combined to form luminescence maps with dimensions of approximately 2 x 3.6 cm, i.e. representing the full surface area of individual thin sections. The terminology applied here to differentiate between different luminescence zones is "non-luminescent/intrinsic", "patchy luminescent" and "bright luminescent" (Fig. 4). This approach allows for very detailed assessment of stratigraphic and spatial changes within and across different cement rims (Fig. 5).

4.2. Geochemistry

All studied rock samples have been analysed for their light stable isotope geochemistry ($\delta^{13}C$ and $\delta^{18}O$). Aliquots were used for the analysis of conventionally used main and trace elemental concentrations. Based on the features observed during cathodoluminescence microscopy, 152 powder sub-samples have been drilled from the corresponding rock slabs. A total of 34 samples are taken from Pennsylvanian red-stained

limestones, while 78 samples have been taken from Upper Triassic reefal limestone and 40 from Upper Cretaceous limestone breccia. A total of 78 samples were analysed from the Upper Triassic comprising 24 general samples and 54 detailed samples from a transect through a 3-cm-thick RFC succession. The approach commonly applied when investigating different paragenetic stages in cement-filled pores is to place a transect across the centre of the pore aiming at a full coverage of all phases. Here we applied a different approach placing a transect across the portions of the pore, where the radiaxial fibrous calcites are thickest and most complete (Fig. 5A).

Additionally, redox-sensitive and rare earth elements of the Triassic cement succession have been measured by means of Laser-Ablation-ICP-MS in order to gain independent information regarding the porewater evolution. Clumped isotope Δ_{47} values (Fig. 5D) of four samples have been performed in order to shed light on the burial history of these samples.

4.2.1. Carbon and oxygen isotope analysis

Based on cathodoluminescence maps, two different sampling approaches have been applied: (i) spatial sampling of carbonate powder from each of the typical CL zones observed using a Dremel hand drilling device with a 0.3 mm diamond drill head. (ii) In order to obtain a time-resolving data set across all paragenetic successions, a geochemical transect (54 data points) of 3 cm length, oriented perpendicular to the main orientation of cement seams, has been drilled from an Upper Triassic rock sample (Rk-1-H) with a computer-controlled CAM milling cutter device. This translates into sampling increments of 18 samples/cm (Fig. 5).

Carbon and oxygen isotope ratios were analysed using a Gasbench coupled to a ThermoFinnigan MAT-253 mass spectrometer at the Ruhr-University Bochum. Carbon and oxygen isotopic ratios are given in ‰ relative to Vienna Pee-Dee Belemnite (VPDB) standard. Carbonate standards CO1, CO8, NBS19 as well as an internal standard were used for correction of the measured values. Prior to analysis, samples of 0.35 to 0.40 mg have been weighed in into glass vials and then dried in an oven with a temperature of about 105°C for 48 hours. Then the glass vials were closed gastight and put into a heated (70°C) autosampling

device and first flushed with He gas in order to remove the atmosphere inside the glass vials. After that a few drops of phosphoric acid are given on the sample and the emerging CO_2 is soaked in and measured for its carbon and oxygen isotopic composition in the coupled mass spectrometer.

4.2.2. Clumped isotope (Δ_{47}) analysis

Four samples of pure RFC aliquots were selected for clumped isotope analysis in order to get information about temperature and burial history. The sample locations have been chosen close to the transect sampled for stable isotope ratios and trace element concentrations, one sample originating in both outermost cement layers (1b/t) as well as two samples in the central layers 4(b/t), where one sample is located on the left side of the transect in a bright luminescent zone and the other one on the right side of the transect in a non-luminescent zone (Fig. 5). Clumped isotope analysis were performed at the Qatar Stable Isotopes Laboratory at Imperial College, London, UK. Six to eight mg of powdered calcite were reacted for 10 minutes in phosphoric acid held at 90°C. The CO_2 gas was purified by passage through a conventional vacuum line with multiple cryogenic traps and a Porapak-Q trap held at -35°C (Dennis and Schrag, 2010). CO_2 gas was analysed using a ThermoFinnigan MAT-253 gas source isotope ratio mass spectrometer configured to measure masses 44 through 49. Analytical protocols and corrections for non-linearity follow Huntington et al. (2009) and the data are reported in the "carbon dioxide equilibrium scale" (CDES) of Dennis et al. (2011). An acid correction factor of +0.069‰ was added to all measurements of $\Delta_{47\ CDES}$ following Guo et al. (2009) and Wacker et al. (2013). Masses 48 and 49 were monitored to check for possible sample contamination following Affek and Eiler (2006) and Huntington et al. (2009; 2011). Each sample was measured four times to improve counting statistics. The $\Delta_{47\ CDES}$ reproducibility is ±0.02 permil based on regular analysis of Carrara marble and an intercalibration carbonate standard ('ETH3'). The Carrara marble $\Delta_{47\ CDES}$ mean value for the measurement period is 0.385±0.016‰ (1SD, n=20) and 0.691±0.017‰ (1SD, n=16) for ETH3. The $\Delta_{47\ CDES}$ values were converted to temperature solving numerically the calibration of Kluge et al. (2015):

$$\Delta_{47}{}^{eq} = 0.98 * \left(\frac{-3.407\,x\,10^9}{T^4} + \frac{2.365\,x\,10^7}{T^3} - \frac{2.607\,x\,10^3}{T^2} - -\frac{5.880}{T}\right) + 0.293 \quad [1]$$

This calibration produced a good linear correlation of all data sets in the Kluge et al. (2015) study and thus confirms that the uncertainty of the acid fractionation correction has no impact on the temperature relationship. Additionally, as the samples of this study were processed, measured and evaluated in the same way as those of Kluge et al. (2015), this calibration is especially valid for this study.

4.2.3. ICP-AES and ICP-MS major and trace elemental analysis

Major and trace elemental abundances (Ca, Mg, Sr, Fe and Mn) of all samples have been analysed making use of an inductively coupled plasma atomic emission spectrometer (ICP-AES) at Bochum. For the translation of the measured values into the unit ppm (parts per million), the certified reference materials BSC-CRM-512 (dolomite) and BSC-CRM-513 (limestone) were analysed. Analytical errors are given as ±%RSD. The 1σ-reproducibility for the major- and trace elements of the two standard materials is: ±0.18% for Ca, ±0.081% for Mg, ±22 ppm for Sr, ±17 ppm for Fe and ±1 ppm for Mn (CRM-512, n=111) and ±0.36% for Ca, ±0.002% for Mg, ±1 ppm for Sr, ±12 ppm for Fe and ±1 ppm for Mn (CRM-513, n=111; Geske et al., 2015).

4.2.4 Laser ablation-ICP-MS minor and rare earth element analyses

Additional minor and rare earth elemental data have been obtained via laser ablation inductively-coupled plasma mass spectrometry (LA-ICP-MS) at the Institute for Mineralogy, Westfaelische Wilhelms-Universität, Münster. Within the limitation of sampling possibilities, this was done in order to collect comparable sample sets from sites that are situated as closely to each other as possible. For the LA-ICP-MS analysis, the sampled rock slice has been cut perpendicular to the drilled profile, turned by 90° and the laser track on the newly cut surface has been aligned as close as possible to the drilled transect (Fig. 5B). Sample ablation was performed with a 193nm ArF excimer laser (Analyte G2, Photon Machines). The repetition rate was set to 10 Hz using a fluence of 4J/cm^2. The beam spot diameter was 110 µm for the entire session.

Ablated particles were transported by helium carrier gas and mixed with argon sample gas before entering the Element 2 (ThermoFisherScientific) single collector mass spectrometer. Forward power was 1300 W and reflected power < 2 W, gas flow rates were 1.1 l/min for total He and 0.9 l/m and 1.2 l/m for the Ar-auxiliary and sample gas, respectively. Cooling gas flow rate was set to 16 l/min. Prior to analyses, the system has been tuned on the NIST 612 reference material measuring ^{139}La, ^{232}Th and $^{232}Th^{16}O$ for high sensitivity and stability and low oxide rates ($^{232}Th^{16}O/^{232}Th$ <0.1%) during ablation. Overall measurement time for a single spot analysis was 60 s, with 20 s for background and 40 s for peak signal. The washout time between two spots was set to 15 s. A total of 47 elements were analysed using ^{43}Ca as internal standard element and NIST 612 as external reference material (Jochum et al., 2011). Distance between single laser spots was 400µm in order to be close to resolution of the profile drilled with the computer-controlled mill along the same cement succession. This resolution yielded 95 data points over a line of 3.8cm. Groups of about 20 unknowns were bracketed with 3 NIST 612 calibration standards to keep track of instrumental drift over the course of the session. Raw data were further processed using the Glitter program (Griffin et al., 2008).

Due to known analytical problems in analysing carbonates with LA-ICP-MS (Jochum et al., 2012), the MACS-3 carbonate reference material provided by the USGS was measured along with the samples to monitor for accuracy and precision. Table A.1 (Appendix) shows that MACS-3 (n=13) trace element concentrations generally match the published range of values given in previous work (Chen et al., 2011; Jochum et al., 2012; Jochum et al., 2014; see GeoRem database version 18) proving that the analytical conditions chosen for this study give reasonably precise and accurate data with average 1-sigma standard deviation in the order of ~14% for concentrations <1ppm, 7% for element concentrations > 1 ppm and approximately 6% for concentrations higher than 100ppm.

Rare earth element values have been normalized to the North American Shale Composites (NASC) values given in McLennan (1989). Cerium-anomalies can be used as an individual paleo-redox proxy and have been calculated using the following equation (Nozaki, 2001), where “N” stands for shale-normalized concentration:

$$Ce / Ce^* = 2Ce_N / (La_N + Pr_N) \quad [2]$$

In order to check Ce-anomalies for their reliability, also the Pr-anomaly has been calculated to be plotted against the Ce-anomaly to construct a La-anomaly diagram following work by Bau and Dulski (1996). For this the following equation has been used:

$$Pr / Pr^* = 2Pr_N / (Ce_N + Nd_N) \quad [3]$$

5. Results

5.1. Petrography and luminescence patterns

All radiaxial fibrous cements studied here reveal spatially complex cathodoluminescence (CL) patterns (Fig. 4). Differential luminescence patterns are recognized stratigraphically, i.e. luminescence patterns change between successive layers, but also laterally within single cement layers (spatially). Luminescence colours range from dark blue and near non-luminescent (intrinsic luminescence; Fig. 4B), via patchy luminescence (intrinsic with yellowish patches or dots; Fig. 4D) to bright yellow or orange-brown (micro-patchy) luminescence colours (Fig. 4F). We here refer to non-luminescent, patchy luminescent, and bright luminescent patterns and have assigned geochemical data accordingly.

Bashkirian (Pennsylvanian) radiaxial fibrous calcite cements from Northern Spain nucleate on red micrite slope carbonates (Fig. 2A) and occlude inter-particle pore space between brachiopod shells, echinoderm fragments, and other bioclasts. They form part of paragenetic successions that, towards the centre of many pores, grade into scalenohedral and then blocky calcites (bright yellow/orange luminescence), locally with internal red sediments (crystal silt). Radiaxial fibrous calcites form fringes that are rather thin when compared to e.g., the Triassic ones. Specifically, individual layers reach some mm in thickness only with several superimposed layers amounting to 2 cm or less. Individual radiaxial fibrous crystals reach length:width ratios between 4:1 and 8:1. A more or less distinct cloudy zonation results from micro-inclusions and is also reflected in the corresponding luminescence patterns. All types of cathodoluminescence patterns used here are present.

From the sample material available, an Upper Triassic (Carnian to Norian) specimen (Rk-1-H; Figs 2B, 5) from Hydra Island (Greece) was selected as a particularly representative case example of a stratigraphically thick succession of consecutive radiaxial calcite layers occluding primary pore space. Sample Rk-1-H is devoid of any mesoscopically visible late burial veining. A significant proportion of the data shown here were taken from this hand specimen. Nucleating on a reefal limestone substratum, sample Rk-1-H included a total of eight cement layers, representing four coeval couplets of cement precipitation (Figs 2B, 5C). All types of cathodoluminescence patterns used here are present. Thin-section microscopy of this rock sample revealed characteristic petrographic changes from the outer cement fringes towards the centre of the pore (Fig. 5C). In the outermost two cement fringes (cement layers 1b and 1t; Fig. 5C), nucleating on the limestone substratum, individual radiaxial calcites reach length:width ratios between 5:1 and 8:1 similar to the Bashkirian ones. Individual crystals display a distinct undulosity and often reveal sub-crystals. In these outer fringes, radiaxial fibrous calcite (RFC) fabrics dominate (>95%) as based on thin section analysis. Single fascicular optical fibrous calcites (FOFC) are found in places but remain volumetrically insignificant (<5%). Cement rims 1b and 1t display well defined, large crystals lacking distinct sub-crystals and undulosity moves smoothly through the crystals when turning the microscope table. Initially, the orientation of individual crystals is at best sub-parallel. With increasing crystal growth, crystal c-axes are oriented increasingly parallel where crystals also show an increasing presence of sub-crystals. The most curved cleavage is present in earliest phases 1b/t and 2b/t but turns increasingly linear in later stages 3 to 4. All layers contain both radiaxial fibrous as well as fascicular optical fabrics. In cement rims 3b/t and 4b/t, i.e., towards the centre of the pore, the fascicular optical fabrics increase in abundance (layer 4b/t >90% FOFC). The Triassic samples display rather dull and dark luminescence features with localized layered as well as patchy areas with bright luminescence. Cement fringes 1t/b are mostly non-luminescent and are followed by two fringes of patchy luminescent radiaxial calcites (2b/t and 3b/t in Fig. 5D). The cement layers close to the suture (4b/t in Fig. 5D) are generally dull luminescent whilst both grade laterally into bright luminescent calcites.

Cenomanian (Upper Cretaceous) samples from Dokos Island (Greece) are characterized by radiaxial calcite cements occluding abundant pore space in outer platform limestone breccia (Fig. 2C). Successions of radiaxial calcite vary in thickness between 1 and 2 cm but paragenetic sequences may reach 5 cm in width locally. In the latter case, radiaxial calcites are, towards the centre of the pore, overlain by blocky, bright luminescent calcite cement assigned to the burial diagenetic realm. Internal sediments are present in some cases. The radiaxial fibrous calcite crystals (length:width ratios of about 4:1) are rather inclusion-rich (cloudy) whilst they lack the distinct zonation than of their Bashkirian counterparts. Generally, they are smaller and thinner compared with crystals from the other samples. The Cenomanian fabrics from Dokos are characterized by two luminescence patterns: (i) patchy yellow luminescence that is well-correlated with individual cement seams, and (ii) bright yellow luminescence, locally superimposed by patches of dull luminescence.

5.2 Geochemistry

5.2.1. Spatially distributed samples: Geochemical properties of luminescence zones

The geochemical data set (Table 2, Figs 6 and 7) is described below in a condensed manner. Bashkirian radiaxial fibrous calcites are typified by rather invariant carbon-isotope values between +4.6 and +5.5‰ (mean = +5.0‰, standard deviation σ = 0.18), whilst oxygen-isotope ratios show a broad range between -5.6 and +2.1‰ (mean = -2.4‰, σ = 2.08; Fig. 6A). Non-luminescent (intrinsic) samples display more positive $\delta^{18}O$ ratios (+2.1 to -3.7‰, mean = -0.7‰) compared to those with patchy (-5.6 to -1.4‰, mean = -3.5‰) or bright yellow luminescence (-5.2 to +1.1‰, mean = -2.7). Magnesium elemental concentrations are slightly enriched in non-luminescent samples (non-luminescent: 7482 to 11770ppm and bright luminescent: 6372 to 9473ppm), whilst Mn concentrations reveal no distinct trend in concentration from non-luminescent to bright luminescent patterns (non-luminescent: 5 to 571ppm, mean = 88ppm and bright luminescent: 14 to 219ppm, mean = 98ppm). Sr elemental abundances show a slightly opposite trend, as they are moderately depleted in bright luminescent samples compared with non-luminescent ones (non-luminescent: 302 to 430ppm, mean=382ppm and bright luminescent: 296 to 694ppm, mean=350ppm). Iron

concentrations show an increase from non- (32 to 366ppm, mean = 103ppm) to bright luminescent cements (25 to 485ppm, mean = 138ppm). In comparison to the two data sets described below, Bashkirian samples yield higher trace element concentrations in terms of Mg, Mn and Sr that show significant variability (Fig. 7).

Upper Triassic radiaxial fibrous cements display a much smaller variability in oxygen (-1.6 to -0.9‰, standard deviation of all Triassic samples $\sigma = 0.29$) and also in carbon isotope ratios (+2.8 to +3.7‰, mean = +3.3‰, $\sigma = 0.16$; Fig. 6B). Bright luminescent samples coincide with lower $\delta^{13}C$ values compared to those characterized by patchy or non-luminescence, while no distinct pattern between luminescence characteristics and $\delta^{18}O$ ratios was observed. Bright luminescent samples yield lower Mg abundances compared to non- and patchy-luminescent calcites. Several studies revealed that luminescence in calcite is mainly caused by incorporation of Mn into the crystal lattice (ten Have and Heijnen, 1985; Habermann et al., 1998; (Richter et al., 2004). As expected, Mn concentrations increase from non- to bright luminescent calcites. Strontium concentrations of non- and patchy-luminescent cements are rather similar but show a decrease towards bright luminescent samples while Fe reveals a moderate increase from non-luminescent over patchy to bright luminescent calcites (Fig. 7).

Cenomanian fibrous cements yield $\delta^{13}C$ ratios ranging between +3.0 and +3.4‰ and a corresponding mean value of +3.2‰ and the standard deviation for all Cenomanian samples is $\sigma = 0.12$. Carbon isotope ratios of bright luminescent samples are lower than those of non-luminescent calcites (Fig. 6C). The corresponding $\delta^{18}O$ values range between -3.2 and -1.2‰ and exhibit a mean value of -2.0‰ and $\sigma = 0.62$. Radiaxial calcites characterized by dark blue luminescence plot in a narrow range ($\delta^{13}C$: +3.3 to +3.4‰, mean = +3.3‰; $\delta^{18}O$: -1.3 to -1.8‰, mean = -1.5‰). Bright luminescent calcites remain invariant in terms of their carbon isotope signatures but are more variable in their $\delta^{18}O$ ratios ($\delta^{13}C$: +3.1 to +3.4‰, mean = +3.2‰; $\delta^{18}O$: -3.2 to -1.2‰, mean = -2.4‰). Oxygen isotope ratios tend to lower values from non- over patchy- to bright luminescent fibrous calcites, whereas some of the samples taken from bright luminescent calcites plot within the range of the non-luminescent samples. Magnesium abundances are rather homogenous but gradually increase from non- to patchy-luminescent cements. Bright luminescent

samples yield moderately depleted Mg concentrations. Manganese concentrations increase from non- to bright luminescent cements. Strontium concentrations display mean values between 178 and 193ppm, with minima found in non-luminescent and maxima in patchy-luminescent cements. Iron concentrations show an increase from non-, to patchy-, to bright luminescent cements (Fig. 7).

5.2.2 Triassic case example: Geochemical transect across different luminescence zones

Magnesium, Mn, Sr, and Fe concentrations (ICP-OES) as well as carbon and oxygen isotope ratios are illustrated in Figure 8. Redox-sensitive element patterns (LA-ICP-MS) and rare earth element patterns are documented in Figures 9 through 12. Generally, the geochemical data acquired from the transect across the paragenetic cement succession display a very prominent symmetrical stratigraphic pattern from cement fringes 1b and 1t towards the central suture of the cement successions (Fig. 8). This geochemical pattern is near-identical in both, up- and downward growing cement successions, a feature considered evidence for a geochemical pattern that reflects pore water properties in a phreatic environment. Three out of four data sets (Mg, Fe, and Sr) and carbon and oxygen isotope values reveal a general trend to more depleted isotope values or decreasing elemental concentrations towards the central suture (Fig. 8). Conversely, Mn elemental abundances become gradually enriched towards the central suture and lack a comparable symmetrical pattern. Higher order patterns are superimposed upon this general trend. Specifically, $\delta^{18}O$, Sr, Mn, and Fe show a spatially limited shift to higher ratios/abundances at the boundary between non-luminescent/intrinsic (1b/t) and (patchy) luminescent (2b/t and 3b/t) cement fringes, albeit with rather variable amplitudes. The most pronounced excursion towards lower values is found in the case of Mg (amplitude: 1450 ppm), whilst oxygen isotope ratios display only a minor shift in the order of 0.5‰ ($\sigma = 0.16$). Carbon isotope ratios and Mg concentrations co-vary. Moreover, geochemical patterns change between cement layers 3b/t and 4b/t. Here, a pronounced decrease in Sr, Mg, and Fe concentrations is observed, while a trend to increasing Mn concentrations is found. The main changes in geochemical patterns, and particularly so with reference to activators (Mn^{2+}) and inhibitors (Fe^{2+}), coincide largely with changes in luminescence characteristics but the issue is complicated by other activator elements such as REE (Richter et al., 2004).

Elements analysed by means of LA-ICP-MS (U, Cd, Zn, and Cu) display the same first order geochemical pattern as observed for Fe, Sr, and Mg concentration analysed by ICP-OES (Figs 8, 9). Specifically, Zn concentrations determined with LA-ICP-MS range between 4.2 and 87ppm (σ = 11.4 ppm) with a mean value of 20.2ppm. Cadmium concentrations range between 0.1 and 1.7ppm (σ = 0.36ppm) with a corresponding mean value of 0.7ppm. Uranium concentrations range between 0.016 and 0.18ppm (mean = 0.06ppm; σ = 0.083ppm). Despite differences in total concentrations of these four elements and therefore also the varying ranges, all of them show a very similar symmetric pattern. Concentrations are generally highest in the outermost cement fringes (1t and 1b; Fig. 5) but decrease in layers 2t/b and increase again in layers 3t/b. Decreasing abundances are found in layers 4t/b.

Figure 10 displays the patterns of shale-normalized REE concentrations from all transect data. All samples are characterized by an overall slight increase in concentrations from light to heavier REE. Distinctly lower Ce concentrations compared to other REE are visible for all samples except one, this phenomenon is called cerium-anomaly (e.g., Alibo and Nozaki, 1999). The calculated Ce anomalies (Ce/Ce*) range between 0.03 and 1.2 with a mean value of 0.17 (Fig. 11). A distinct increase in Ce-anomaly is present in cement layers 4b and t, respectively. Values in the middle part vary between 0.08 and 1.2 and one maximum value of 1.2 while in the outer cement layers (1 t/b to 3 t/b) are mostly below 0.3.

Clumped isotope Δ_{47} values of four radiaxial calcite samples from Hydra suggest temperatures between 179°C and 202°C. Specifically, the sample taken from the earliest cement rim 1b has a Δ_{47} value of 0.422±0.023‰, suggesting a calculated temperature of 199±31°C. The sample from the coeval cement rim 1t displays a Δ_{47} value of 0.420±0.006‰ translating into a calculated temperature of 202±7°C. The two samples taken from layer 4b/t, i.e. the latest phase precipitated, yield Δ_{47} values of 0.431±0.019‰ (bright luminescent) and 0.439±0.007‰ (n.l.) corresponding to temperatures of 188±24°C (bright luminescent) and 179±8°C (non-luminescent). Within the limitations of 1SD, the calculated temperatures are identical (mean: 192±11). In order to further evaluate the clumped isotope data, conventional $\delta^{18}O$ and $\delta^{13}C$ values, and such from the clumped analysis are compared. Carbon isotope values of the clumped isotopes method yield constant values with low uncertainties (~ 0.06‰,) and are in very good agreement with the values analysed

using the MAT253 GasBench. Oxygen isotope ratios derived from clumped isotope measurements show higher uncertainties (~0.45‰) but are in agreement with those measured with the MAT253 GasBench approach.

6. Interpretation and Discussion

The main focus of this study is to re-evaluate the potential of time-resolved successions of radiaxial fibrous calcites as archives of their marine to burial diagenetic pathways. In order to achieve this, we compared spatially randomly distributed samples with those collected along a specific cement succession. A first important step is the subdivision of patterns assigned to different diagenetic stages. This is undertaken by assessing isotope data in the context of the cathodoluminescence patterns of the specific sample material and by comparing data shown here with previous work.

6.1. Spatially distributed samples: Marine porewater diagenesis and comparison to published data sets

The comparison of luminescence characteristics and isotope data from all samples reveals a significant pattern (Fig. 6). The most obvious relation between non-, patchy and bright luminescent calcites and isotope values is found in the Pennsylvanian data set, specifically with reference to oxygen isotopes (Fig. 6A). As commonly inferred (e.g., Bruhn et al., 1995; Kaufmann and Wendt, 2000), increasing luminescence patterns point to reducing conditions during burial favouring Mn^{2+} incorporation in the crystal lattice and agree with decreasing oxygen isotope values corresponding to increasingly warm pore fluids. The Upper Triassic data set is characterized by narrow oxygen and moderately variable carbon isotope ratios being clearly related to luminescence (Fig. 6B). Upper Cretaceous samples display moderately ^{18}O enriched oxygen isotope values of non-luminescent, relative to luminescent cements, and near-invariant carbon isotope ratios. Two preliminary conclusions can be drawn: (i) Luminescence patterns are in rather good agreement with isotope data, mainly with reference to oxygen and less clearly to carbon isotope ratios. (ii)

It seems that the general assignment of bright luminescence as a priori diagenetic geochemical signature is not always true and has to be evaluated for every sample by a careful comparison of different data.

Following previous work of Tobin et al. (1996), the isotope patterns observed here for samples of different time periods are perhaps best explained by cementation and subsequent small-scale dissolution/reprecipitation during early diagenetic, shallow marine burial. Corresponding fluids are thought to be still marine to modified marine in origin except for bright luminescent samples from Pennsylvanian where burial fluids seem dominant. This is indicated by the considerable scatter in oxygen isotope values and the corresponding high calculated temperatures. The temperature equation used here in order to assess $\delta^{18}O$ derived fluid temperatures is that of Grossman (2012; derived from Kim and O'Neil, 1997). Patchy to bright luminescent Pennsylvanian cements translate into fluid temperatures between 15 and 37°C, pointing to shallow burial diagenesis. Pennsylvanian non-luminescent samples, on the other hand, reveal calculated fluid temperatures from $\delta^{18}O$ values ranging from 1 to 26°C with a mean value of ~12°C.

Conversely, applying the same quation to the Upper Triassic samples, calculated fluid temperatures range between 13 and 16°C (a $\delta^{18}O_{water}$ of -1 has been used, assuming an ice-free world), i.e., a range indicative of the normal marine domain. Calculated fluid temperatures from Cretaceous samples vary between ~14 and 24°C. Summing up, the data compiled here are, according to conventional interpretations, is best understood in the context of diagenetic stabilisation of a high-Mg radiaxial fibrous calcite precursor phase under very early marine burial conditions. Evidence for a significant later burial overprint is not found. An exception is found in the case of a bright luminescent zone (Fig. 5C; 4b/t, left) in portions of the centre of the cement-filled pore space in the Triassic case example. Specifically, the bright luminescent zone is related to an area with abundant fracturing and dense burial veining. Whilst the veins are filled with orange-brown luminescent cement, the radiaxial fibrous cement is altered and portions replaced by orange-brown and yellow luminescent phases.

When comparing the RFC carbon and oxygen isotope data presented in this study with estimates of coeval marine seawater values published in previous work, we obtain the following results. Hasiuk and Lohmann (2008) document, in comparison to data shown here, ^{13}C depleted carbon isotope ratios for

505 Mississippian (Tournaisian–Visean) marine radiaxial fibrous cements. The meaning of this is difficult to
506 assess and the problem of comparing data from different epochs of the Carboniferous, and from different
507 settings, is acknowledged here.

508 Conversely, calcite $\delta^{13}C$ and $\delta^{18}O$ isotope ratios shown here are either in the same range or enriched
509 relative to previous data (Fig. 6; e.g., Bruckschen et al., 1999; Veizer et al., 1999). Specifically, non-
510 luminescent samples of Pennsylvanian and all samples of Upper Triassic radiaxial calcites plot towards the
511 ^{13}C and ^{18}O enriched range of these data sets (Fig. 6). Conversely, the Upper Cretaceous ones agree in terms
512 of their $\delta^{18}O$ range but are enriched in ^{13}C relative to those shown in Bruckschen et al. (1999) and Veizer et
513 al. (1999). Having said this, it must be noted that the data shown in Bruckschen et al. (1999) and Veizer et
514 al. (1999) heavily rely on biogenic marine carbonate archives (skeletal carbonates; e.g., brachiopod shells)
515 that should not be compared with inorganic precipitates in a non-critical manner (Immenhauser et al., 2015).

516 Summing up, the bulk of published data on radiaxial calcites from the time slices discussed here is
517 remarkably small, too small to allow for a more systematic comparison. Moreover, only a limited number
518 of the studies published compare geochemical data with luminescence properties of these cements.

519

520

521 *6.2. Relation of calcite elemental concentrations to luminescence properties*

522 Elemental data reveal increasingly depleted Sr and Mg concentrations from non- via patchy to bright
523 luminescent cements. Both of these elements are commonly enriched in marine abiogenic precipitates and
524 consequently, depletion of these elements is usually assigned to secondary diagenetic controls (e.g., Brand
525 and Veizer, 1980; Satterley et al., 1994). Depletion in Sr and Mg coincides with an increase in Mn (activator)
526 and Fe (quencher) concentrations of cements with increasing luminescence, the latter is usually assigned to
527 burial diagenesis (~1 ppm in abiotic marine precipitates under oxic conditions; Major and Wilber, 1991
528 versus >400ppm Mn in cements indicative of anoxic, non-marine fluids; Bruckschen et al., 1999). Satterley
529 et al. (1994) suggest, that marine carbonates yield concentrations of less than 100 ppm Fe and less than 10
530 ppm Mn. Considering the concentrations measured in the radiaxial cements studied here, exchange of

calcites with marine burial porewater seems likely. Tobin et al. (1996) describe radiaxial fibrous calcite cements from the Ordovician of Tennessee with Mn concentrations of ≤10,000 ppm and patchy luminescence patterns and associate these elemental values and luminescence patterns to overprint of a marine magnesian calcite precursor phase under reducing diagenetic conditions. For comparison, elemental data shown in this study have maximum values of 600 ppm Mn but more commonly range between some tens to a few hundred ppm (Fig. 7). Increasingly bright luminescence is assigned to increasing calcite Mn concentrations but values must not necessarily reach those considered indicative for diagenetic overprint under sub- or anoxic burial conditions. Specifically, the hot cathode device used in the context of this study is very sensitive to Mn and probably highlights patterns in Mn concentrations related to precipitation kinetics (Habermann et al., 1998) if not quenched by iron (ten Have and Heijnen, 1985) as discussed for the case example of Fe below.

A similar pattern is found in the case of Fe elemental concentrations. Specifically, Tobin et al. (1996) describe luminescent radiaxial fibrous calcites of Ordovician age with mean Fe concentrations of ≤2000 ppm (400ppm and less for non-luminescent phases). Conversely, data presented in figure 7 show Fe concentrations of less than 500 ppm, with most values remaining below 250 ppm. Ten Have and Heijnen (1985) argue that where calcite iron concentrations remain below 200ppm, luminescence induced by Mn is not quenched. Based on precipitation experiments, ten Have and Heijnen (1985) documented that it is rather the absolute amount of calcite Mn^{2+}, as opposed to the Fe^{2+}/Mn^{2+} ratio, and equally important, changes in the rate of crystal growth that affect luminescence zonations. This implies that kinetic factors (e.g., calcite growth rates) interact in a complex manner with environmental ones (e.g., fluid chemistry). In the context of the paragenetic succession studied here, it seems more than likely that growth rates of successive generations of radiaxial calcites changed with time. The highest growth rates are expected during the early stages of radiaxial fibrous cement formation (i.e., phase 1b/t in Fig. 5) when the water circulation in the pore space is vigorous due to wave and current action. Under increasing cementation of pore space and related clogging of fluid circulation pathways, precipitation/recrystallization rates continuously decrease.

Generally the relation between Fe concentrations and degree of luminescence is present but weak in the data set shown here. Comparing different data sets from radiaxial fibrous calcite of different time intervals and basins, however, is not straightforward. Besides differences in the geochemistry of Pennsylvanian, Upper Triassic, and Upper Cretaceous seawater and related element distribution coefficients, perhaps even subtle patterns in diagenetic fluid chemistry, burial depth, and rate or non-equilibrium factors represent important factors (e.g., Reeder and Grams, 1987; Barnaby and Rimstidt, 1989; Rimstidt et al., 1998).

Two preliminary conclusions can be drawn after the previously described observations. (i) The general elemental patterns found in all three case examples agree with marine (porewater) radiaxial magnesian calcites that were subject to only very moderate diagenetic overprint under slightly reducing conditions. The main source of the fluids remained seawater except for patchy and bright luminescent samples of Pennsylvanian that have seen higher degrees of alteration under non-marine fluid influence. This notion agrees with conclusions previously drawn from the light stable isotope data documented here. (ii) Elemental concentrations are reflected, at least to some degree, in the luminescence patterns of the corresponding cements.

6.3. Radiaxial fibrous calcites as archives of diagenetic pathways: Application of less-conventional proxies

Having tentatively established, by means of conventional proxies for fluid properties, the low degree of diagenetic alteration of the calcite cements documented here, we now discuss the implications of the less-conventional proxy data compiled in the transect data across radiaxial calcites in the Upper Triassic specimen Rk-1-H (Figs 5 and 8 through 12). Additionally, we reconstruct a simple example for the diagenetic history of the cement succession and construct a model for cement paragenesis in the analysed Upper Triassic reefal limestone (Fig. 13).

Δ_{47} values of all four samples analysed are comparatively low and fall between 0.420 and 0.439‰. This is only marginally higher than the Δ_{47} value of Carrara marble measured in the same analytical session

582 (~0.395‰) and suggests a high-temperature origin of the sample clumped isotope signature (Kluge et al.,
583 2015). Using Eq. 1, the fluid temperature estimates suggested by clumped isotope data from the Upper
584 Triassic sample Rk-1-H stand in remarkable contrast to temperature estimates based on conventional $\delta^{18}O$
585 data using the temperature equation of Grossman (2012). Specifically, the $\delta^{18}O$ ratios of the calcite layers
586 4t/b, i.e. the last recorded precipitates suggest a maximum fluid temperature of <20°C whilst those indicated
587 by the clumped isotope thermometer applied to the same sample point to temperatures between 178 and
588 202°C. If these temperatures are taken to represent a direct recrystallization of the calcite, and assuming a
589 temperature/depth gradient of 25°C/km (Fridleifsson et al., 2008), a burial depth of ~7-8 km is necessary to
590 explain the data, whilst shallower depths of about 6-7 km or less are necessary when a gradient of 30°C/km
591 is taken. In any case, a burial depth of several kilometres in the context of the thrusting of tectonic naps
592 (Römermann, 1969; Richter, 1999) that now build Hydra Island is likely. During recrystallization, the "true"
593 temperature is recorded in Δ_{47}, irrelevant how fast the uplift was. Uplift or cooling rates only become
594 relevant when solid-state diffusion within crystals is assumed (Passey and Henkes, 2012; Stolper and Eiler,
595 2015). Thus, a Δ_{47} value between the closure temperature of clumped isotopes (~100°C; Henkes et al., 2014)
596 and the maximum burial temperature is expected. Assuming slow uplift rates and related slow cooling of
597 the carbonate successions studied here, the clumped isotope temperatures are largely in agreement with
598 earlier findings by Gillhaus et al. (1999) from Hydra Island reporting the outcome of different temperature
599 proxies (e.g., illite crystallinity, authigenic albites, chert maturity) that suggest burial temperatures between
600 135 and 210°C.

601 The discrepancy of two isotope-based palaeo-thermometers as observed here is remarkable but not
602 unique as such. A prominent example is found in the case of Carrara marble, having seen peak temperatures
603 in excess of 200°C (Vaselli et al., 2012) whilst being characterized by marine $\delta^{13}C$ ratios of +1.5 to +3‰
604 and $\delta^{18}O$ ratios of -0.2 to -3.5‰ (Herz and Dean, 1986). The underlying reasons are not easily understood
605 but perhaps best explained in the context of solid-state resetting (Passey and Henkes, 2012). Nevertheless,
606 numerous workers have documented that marine calcites in the presence of a reducing burial pore fluid with
607 significantly elevated temperatures undergo dissolution-reprecipitation (recrystallization) and exchange via

608 diffusion (Watson and Baxter, 2007) leading mainly to ^{18}O depleted values. In the absence of a fluid phase,
609 however, calcite $\delta^{18}O$ ratios might be locked whilst the ^{13}C-^{18}O bond reordering responds to the elevated
610 temperatures (e.g., Henkes et al., 2014).

611 The concept of burial in the absence of significant amounts of fluids, however, is not easily
612 understood. On the level of a tentative working hypothesis, it is possible that marine radiaxial calcites
613 occluded all of the available pore space and hence, fluid circulation in these tight limestones was reduced
614 to a degree that fluid-carbonate interaction was a surficial rather than a volume phenomenon. This concept
615 is in agreement with the conspicuous absence of genuine burial phases such as blocky calcites or saddle
616 dolomites along the sampled transect that focussed on radiaxial fibrous calcites (Fig. 5). Essentially, some
617 open pore space was present when entering the burial domain as documented in the central portions of the
618 hand specimen shown in figure 5, but not in the sampled part of the specimen. The hypothesis that significant
619 rock-fluid interaction was absent during most of the burial history of the studied sample is also supported
620 by the spatially very limited alteration zone observed in luminescence zones 4b/t. Here, late burial fluids
621 circulated along small veins and affected only a limited portion of the fibrous calcites (Fig. 5C).

622 A second remarkable observation is found in the patterns of redox-sensitive elements, particularly
623 Zn, Cd, U and Cu (Fig. 9). Following previous workers (Thomson et al., 1995; Morford and Emerson, 1999;
624 Tribovillard et al., 2006; Pattan and Pearce, 2009) enriched elemental concentrations of these elements point
625 to increasingly reducing fluids. According to the data shown here, the fluid oxygen level reached highest
626 values in cement phases 2b and 2t and in the late stage phases 4b and 4t (Fig. 9). This seems counter-intuitive
627 given that pore fluids at a depth of a few mm to few cm in the sediment column reach the methanogenic
628 diagenetic stage due to rapid respiration of organic matter (see discussion in Immenhauser et al., 2008).
629 Additional evidence, that might shed light on the processes involved, comes from Mn elemental trends (Fig.
630 8) and REE data (Fig. 10) compiled across the same transect.

631 Essentially, Mn concentrations are stable in cement phase 1t/b and then gradually increase towards the
632 central suture (Fig. 8). This is the pattern expected from a gradually decreasing fluid E_h favouring Mn^{2+} as
633 the dominant species (Bruckschen and Richter, 1994). A similar but less distinct gradual behaviour is only

observed for calculated Ce-anomalies which also points to gradually reducing conditions of radiaxial fibrous calcite formation (i.e., the stabilisation of a precursor phase). Especially, the fully marine cement generations 1b and 1t (Fig. 8) reflect well oxygenated seawater with a dominantly incompatible Mn^{4+} phase. At the onset of generation 2b/t, Mn incorporation in the crystal lattice increases due to increasingly reducing porewater chemistry characterized by Mn^{2+}. Elements like Zn, Cd, U and Cu are often considered to reflect fluid Eh. If true, this would imply oxidized pore fluids for the last cement generation precipitated. The controversial patterns found in Zn, Cd, U, and Cu could be related to non-equilibrium processes, especially with respect to variations in growth rates that strongly affect the incorporation of these elements in the calcite crystal lattice. In addition, it seems possible that some of the redox sensitive elements are less mobile (distribution coefficients) and more difficult to incorporate in the calcite lattice.

Rare earth element patterns (Fig. 10) display an upward enrichment trend towards the heavier REEs, a feature indicative for precipitation from marine fluids. Given that all cement phases display the typical REE pattern of seawater with a well-developed negative Ce-anomaly for most of them, except one (Fig. 10; Lécuyer et al., 2004; Olivier and Boyet, 2006; Bodin et al., 2013), it seems likely that the stabilization from an initially precipitated marine magnesium-rich radiaxial fibrous calcite to a more Mg-depleted phase took place at an early burial stage in the presence of marine pore fluids.

Paleo-redox conditions can also be inferred from evolution of the Ce-anomaly (Ce/Ce*, Fig. 11). Ce/Ce* values fluctuate around a value of 0.1 across cement layers 1b-3b and across cement layers 1t-3t. A value of 0.4 is representative for modern open-ocean shallow oxygenated seawater and probably also for Mesozoic seawater (Shields and Webb, 2004; Bodin et al., 2013). At the onset of cement rims 4b/t, Ce anomaly shifts distinctly towards values around 0.3, indicative for slightly more reducing conditions compared to the other cement phases, but still indicative for oxygenated waters.

In order to check whether the calculated Ce anomalies are due to a genuine depletion of Ce and not a positive La anomaly, the Pr-anomaly (Pr*) has been calculated and plotted against the Ce-anomaly which is then called La-anomaly plot, as suggested by Bau and Dulski (1996) (Fig. 12). This diagram helps to differ if a Ce-anomaly is of genuine nature or if it is caused by anomalous behaviour of other REEs. Data

660 that plots in field IIIb, as the vast majority of our data do, show real Ce-anomalies. Only a few data points
661 do not plot in this field. The one data point that plots in field IIIa can be assigned to the maximum value of
662 Ce-anomalies (a positive Ce-anomaly) and originates in the sampling of the burial vein that crosscuts the
663 sampled cement transect. Plotting in the IIIa field however indicates that this is without a doubt a genuine
664 positive Ce anomaly. Six out of the total of 94 data points plot in field IIa of the Bau and Dulski (1996) plot
665 and may thus be related to anomalous enrichment/depletion of neighbouring elements. Those have been
666 closely examined for their individual REE patterns and we tend to conclude from this examination that also
667 for these samples a genuine negative Ce-anomaly can be assumed. Their slightly different behaviour can
668 rather be linked to a slightly depleted Pr content compared to the other patterns than to any anomalous
669 enrichment in La. We thus conclude that all Ce anomalies calculated here are genuinely related to
670 depletion/enrichment of Ce content relative to the other REE. Even if we exclude the six samples plotting
671 in the IIa field, no significant change in the Ce anomaly trend along the cement phases can be observed.
672 Assuming that these data and interpretations are valid, pore fluids did not reach fully anoxic
673 conditions during late stage radiaxial calcite precipitation or diagenetic stabilization in the studied transect.
674 Summing up, Mn and REE monitored paleo-redox conditions of the pore water suggesting initial radiaxial
675 fibrous cement precipitation (1b/t) under highly oxidizing seawater conditions. These early cement seams
676 are followed by radiaxial fibrous cement precipitation under increasingly reducing conditions but a still
677 near-marine porewater. Other redox-sensitive proxies, and particularly Cd, Zn, Cu and U, appear to be
678 dominated by kinetic factors rather than porewater Eh.
679
680 **7. Conclusions**
681
682 Marine radiaxial fibrous calcites in Pennsylvanian, Upper Triassic, and Upper Cretaceous reefal limestones
683 are re-evaluated as archives of past seawater properties. Based on cathodoluminescence maps, fabrics are
684 subdivided into non-, patchy- and bright luminescent types. There is a moderate agreement between isotope
685 ratios and luminescence with all data plotting in the heavy side of reconstructed coeval seawater isotope

686 data. The commonly held notion that luminescent radiaxial calcites represent substantial diagenetic
687 overprint represents an oversimplification. This as redox properties of (modified) marine porewater and
688 kinetic effects (precipitation rates) affect the incorporation of activating elements in the crystal lattice and
689 may result in the direct precipitation of luminescent radiaxial calcites in open pore space during initial burial.
690 Geochemical patterns along an Upper Triassic transect oriented along the growth directions of the
691 cement layers display a symmetrical stratigraphic pattern from outer cement fringes towards the central
692 suture. Three out of four data sets (Mg, Fe and Sr) and carbon and oxygen isotope values trend to more
693 depleted isotope values or decreasing elemental concentrations towards the central suture. Conversely, Mn
694 elemental abundances become gradually enriched. Redox-sensitive elements such as Zn, Cd, U, and Cu only
695 in partly reflect porewater Eh whereas but more prominently kinetic factors. Conversely, Mn as well as Ce
696 indicate oxic marine porewaters with a shift to moderately sub-oxic conditions and a decreasing influence
697 of marine porewaters towards the latest stage radiaxial calcite precipitation.
698 Contrasting information is obtained from the comparison of two palaeothermometers: $\delta^{18}O$ ratios
699 (<20°C) and clumped isotope geochemistry (180 to 200°C). This controversy is perhaps best understood in
700 the context of solid-state ^{13}C-^{18}O bond reordering in a burial setting under low fluid:rock ratios. REE patterns
701 of all radiaxial calcite phases, suggest that these fabrics stabilized under the influence of increasingly oxygen
702 depleted marine to altered marine porewaters at (shallow marine) burial depths but then ceased to record the
703 subsequent burial history. Essentially, carbonate clumped isotope data represent the only proxy shown here
704 that provides evidence of deeper burial conditions. This observation has general significance for
705 palaeotemperature reconstructions of ancient marine carbonates.
706 The data presented here underline that the application of a multi-proxy data set including – with
707 reference to radiaxial fibrous calcites - less conventional approaches reveals new and important insight into
708 shallow (marine) to deep burial processes. The question whether radiaxial fibrous cement fabrics,
709 precipitated from sub-oxic (altered) shallow marine burial fluids still qualify as marine cements *sensu stricto*
710 merits consideration. This question seems adequate as petrographically, these fabrics are near-identical to
711 fully marine radiaxial calcites.

Acknowledgements

This study was performed in the context of the collaborative research initiative CHARON (DFG Forschergruppe 1644). We acknowledge contributions by R. Neuser for assistance and instruction on the cathodoluminescence. The authors thank the staff of the laboratory for isotope geochemistry at Ruhr-University Bochum and F. Wiethoff, O. Kwiecien, and S. Breitenbach for fruitful discussions.

References

Affek, H.P., Eiler, J.M., 2006. Abundance of mass 47 CO 2 in urban air, car exhaust, and human breath. Geochimica et Cosmochimica Acta, 70: 1-12.

Aissaoui, D.M., 1988. Magnesian calcite cements and their diagenesis - dissolution and dolomitization, Mururoa Atoll. Sedimentology, 35: 821-841.

Alibo, D.S., Nozaki, Y., 1999. Rare earth elements in seawater: particle association, shale-normalization, and Ce oxidation. Geochimica et Cosmochimica Acta, 63: 363-372.

Bahamonde, J.R., Colmenero, J.R., Vera, C., 1997. Growth and demise of Late Carboniferous carbonate platforms in the eastern Cantabrian Zone, Asturias, northwestern Spain. Sedimentary Geology, 110: 99-122.

Bahamonde, J.R., Merino-Tomé, O.A., Heredia, N., 2007. A Pennsylvanian microbial boundstone-dominated carbonate shelf in a distal foreland margin (Picos de Europa Province, NW Spain). Sedimentary Geology, 198: 167-193.

Barnaby, R.J., Rimstidt, J.D., 1989. Redox conditions of calcite cementation interpreted from Mn and Fe contents of authigenic calcites. Geological Society of America Bulletin, 101: 795-804.

Bathurst, R., 1959. The cavernous structure of some Mississippian Stromatactis reefs in Lancashire, England. The Journal of Geology: 506-521.

Bau, M., Dulski, P., 1996. Distribution of yttrium and rare-earth elements in the Penge and Kuruman iron-formations, Transvaal Supergroup, South Africa. Precambrian Research, 79: 37-55.

744 Bernasconi, S.M., Schmid, T.W., Grauel, A.-L., Mutterlose, J., 2011. Clumped-isotope geochemistry of
745 carbonates: a new tool for the reconstruction of temperature and oxygen isotope composition of
746 seawater. Applied Geochemistry, 26: 279-280.
747 Bodin, S., Godet, A., Westermann, S., Föllmi, K.B., 2013. Secular change in northwestern Tethyan water-
748 mass oxygenation during the late Hauterivian–early Aptian. Earth and Planetary Science Letters,
749 374: 121-131.
750 Brand, U., Veizer, J., 1980. Chemical diagenesis of a multicomponent carbonate system - 1. Trace elements.
751 Journal of Sedimentary Petrology, 50: 1219-1236.
752 Bruckschen, P., Oesmann, S., Veizer, J., 1999. Isotope stratigraphy of the European Carboniferous: proxy
753 signals for ocean chemistry, climate and tectonics. Chemical Geology, 161: 127-163.
754 Bruckschen, P., Richter, D., 1994. Zementstratigraphische Grundmuster in marinen Karbonatablagerungen
755 des Phanerozoikums–ein Abbild der normalen Beckenentwicklung. Zbl Geol Paläaont Teil I, 1993:
756 959-972.
757 Bruhn, F., Bruckschen, P., Richter, D.K., Meijer, J., Stephan, A., Veizer, J., 1995. Diagenetic history of
758 sedimentary carbonates - constraints from combined cathodoluminescence and trace-element
759 analysis by Micro-PIXE. Nuclear Instruments & Methods in Physics Research Section B-Beam
760 Interactions with Materials and Atoms, 104: 409-414.
761 Budd, D.A., Frost, E.L., Huntington, K.W., Allwardt, P.F., 2013. Syndepositional deformation features in
762 high-relief carbonate platforms: long-lived conduits for diagenetic fluids. Journal of Sedimentary
763 Research, 83: 12-36.
764 Carpenter, S.J., Lohmann, K.C., 1989. Delta-O-18 and Delta-C-13 variations in Late Devonian martine
765 cements from the Golden Spike and Nevis Reefs, Alberta, Canada. Journal of Sedimentary
766 Petrology, 59: 792-814.
767 Chen, L., Liu, Y., Hu, Z., Gao, S., Zong, K., Chen, H., 2011. Accurate determinations of fifty-four major
768 and trace elements in carbonate by LA–ICP-MS using normalization strategy of bulk components
769 as 100%. Chemical Geology, 284: 283-295.
770 Clift, P.D., 1996. Accretion tectonics of the Neotethyan Ermioni Complex, Peloponessos, Greece. Journal
771 of the Geological Society, 153: 745-757.
772 Clift, P.D., Robertson, A.H.F., 1990. Deep-water basins within the Mesozoic carbonate platform of Argolis,
773 Greece. Journal of the Geological Society, 147: 825-836.
774 Colmenero, J., Fernández, L.P., Moreno, C, Bahamonde, J.R., Barba, P., Heredia, N., González, F., 2002.
775 Carboniferous. The Geology of Spain, 93: 116.
776 Davies, G.R., Nassichuk, W.W., 1990. Submarine cements and fabrics in Carboniferous to Lower Permian,
777 reefal, shelf margin and slope carbonates, northwestern Ellesmere Island, Canadian Arctic
778 Archipelago. Energy, Mines, and Resources Canada.
779 Della Porta, G., Kenter, J.A.M., Bahamonde, J.R., 2004. Depositional facies and stratal geometry of an
780 Upper Carboniferous prograding and aggrading high-relief carbonate platform (Cantabrian
781 Mountains, N Spain). Sedimentology, 51: 267-295.
782 Della Porta, G., Webb, G.E., McDonald, I., 2015. REE patterns of microbial carbonate and cements from
783 Sinemurian (Lower Jurassic) siliceous sponge mounds (Djebel Bou Dahar, High Atlas, Morocco).
784 Chemical Geology, 400: 65-86.
785 Dennis, K.J., Affek, H.P., Passey, B.H., Schrag, D.P., Eiler, J.M., 2011. Defining an absolute reference
786 frame for 'clumped' isotope studies of CO2. Geochimica et Cosmochimica Acta, 75: 7117-7131.
787 Dennis, K.J., Schrag, D.P., 2010. Clumped isotope thermometry of carbonatites as an indicator of diagenetic
788 alteration. Geochimica et Cosmochimica Acta, 74: 4110-4122.
789 Fridleifsson, I.B. et al., 2008. The possible role and contribution of geothermal energy to the mitigation of
790 climate change, IPCC scoping meeting on renewable energy sources, proceedings, Luebeck,
791 Germany. Citeseer, pp. 59-80.
792 German, C.R., Elderfield, H., 1990. Application of the Ce anomaly as a paleoredox indicator: the ground
793 rules. Paleoceanography, 5: 823-833.
794 German, C.R., Holliday, B.P., Elderfield, H., 1991. Redox cycling of rare earth elements in the suboxic zone
795 of the Black Sea. Geochimica et Cosmochimica Acta, 55: 3553-3558.

Geske, A., Lokier, S., Dietzel, M., Richter, D.K., Buhl, D., Immenhauser, A., 2015. Magnesium isotope composition of sabkha porewater and related (Sub-) Recent stoichiometric dolomites, Abu Dhabi (UAE). Chemical Geology, 393: 112-124.

Gillhaus, A., Götte, T., Pletz, A., Richter, D.K., Sedlmayr, N., Wentzler, S., 1999. Zur höhergradigen Diagenese in der permisch/ju rassischen Schichtenfolge von Hydra, Griechenaldn. BeitraÈge zur Sedimentologie von Griechenland I. Bochumer geol. geotech. Arb, 53: 107-125.

Gray, A.F., Adams, A.E., 1995. Sheet voids and radiaxial fibrous calcite cement fills from Upper Jurassic beachrock, Calcaires-Blancs-de-Provence, Southeast France. Carbonates and Evaporites, 10: 252-260.

Griffin, W., Powell, W., Pearson, N., O'Reilly, S., 2008. GLITTER: data reduction software for laser ablation ICP-MS. Laser Ablation-ICP-MS in the earth sciences. Mineralogical association of Canada short course series, 40: 204-207.

Grossman, E.L., 2012. Applying oxygen isotope paleothermometry in deep time, Paleontological Society Papers. Paleontological Society, 39-67.

Guo, W., Mosenfelder, J.L., Goddard, W.A., Eiler, J.M., 2009. Isotopic fractionations associated with phosphoric acid digestion of carbonate minerals: insights from first-principles theoretical modeling and clumped isotope measurements. Geochimica et Cosmochimica Acta, 73: 7203-7225.

Habermann, D., Neuser, R.D., Richter, D.K., 1998. Low limit of Mn2+-activated cathodoluminescence of calcite: state of the art. Sedimentary Geology, 116: 13-24.

Hasiuk, F.J., Lohmann, K.C., 2008. Mississippian paleocean chemistry from biotic and abiotic carbonate, Muleshoe Mound, Lake Valley formation, New Mexico, USA. Journal of Sedimentary Research, 78: 147-160.

Henkes, G.A., Passey, B.H., Grossman, E.L., Shenton, B.J., Pérez-Huerta, A., Yancey, T.E., 2014. Temperature limits for preservation of primary calcite clumped isotope paleotemperatures. Geochimica et Cosmochimica Acta, 139: 362-382.

Herz, N., Dean, N.E., 1986. Stable isotopes and archaeological geology: the Carrara marble, northern Italy. Applied Geochemistry, 1: 139-151.

Hood, A.v.S., Wallace, M.W., 2012. Synsedimentary diagenesis in a Cryogenian reef complex: Ubiquitous marine dolomite precipitation. Sedimentary Geology, 255: 56-71.

Huntington, K., Eiler, J.M., Affek, H.P., Guo, W., Bonifacie, M., Yeung, L.Y., Thiagarajan, N., Passey, B.H., Tripati, A., Daëron, M., 2009. Methods and limitations of 'clumped'CO2 isotope (Δ47) analysis by gas-source isotope ratio mass spectrometry. Journal of Mass Spectrometry, 44: 1318-1329.

Huntington, K.W., Budd, D.A., Wernicke, B.P., Eiler, J.M., 2011. Use of clumped-isotope thermometry to constrain the crystallization temperature of diagenetic calcite. Journal of Sedimentary Research, 81: 656-669.

Huntington, K.W., Lechler, A.R., 2015. Carbonate clumped isotope thermometry in continental tectonics. Tectonophysics, 647: 1-20.

Immenhauser, A., Holmden, C., Patterson, W.P., 2008. Interpreting the carbon-isotope record of ancient shallow epeiric seas: lessons from the Recent. Dynamics of epeiric seas, 48: 135-174.

Immenhauser, A., Schöne, B.R., Hoffmann, R., Niedermayr, A., 2015. Mollusc and brachiopod skeletal hard parts: intricate archives of their marine environment. Sedimentology.

Jacobshagen, V., 1986. Geologie von Griechenland, 19. Gebruder Borntraeger Verlagsbuchhandlung.

Jochum, K.P., Scholz, D., Stoll, B., Weis, U., Wilson, S.A., Yang, Q., Schwalb, A., Börner, N., Jacob, D.E., Andreae, M.O.., 2012. Accurate trace element analysis of speleothems and biogenic calcium carbonates by LA-ICP-MS. Chemical Geology, 318: 31-44.

Jochum, K.P., Stoll, B., Weis, U., Jacob, D.E., Mertz-Kraus, R., Andreae, M.O., 2014. Non-Matrix-Matched Calibration for the Multi-Element Analysis of Geological and Environmental Samples Using 200 nm Femtosecond LA-ICP-MS: A Comparison with Nanosecond Lasers. Geostandards and Geoanalytical Research, 38: 265-292.

Jochum, K.P., Weis, U., Stoll, B., Kuzmin, D., Yang, Q., Raczek, I., Jacob, D.E., Stracke, A., Birbaum, K., Frick, D.A., 2011. Determination of reference values for NIST SRM 610–617 glasses following ISO guidelines. Geostandards and Geoanalytical Research, 35: 397-429.

Kaufmann, B., 1997. Diagenesis of middle Devonian carbonate mounds of the Mader basin (eastern Anti-Atlas, Morocco). Journal of Sedimentary Research, 67: 945-956.

Kaufmann, B., Wendt, J., 2000. Calcite cement successions in Middle Devonian (Givetian) carbonate mud buildups of the Southern Ahnet Basin (Algerian Sahara). Carbonates and Evaporites, 15: 149-161.

Kendall, A.C., 1976. Origin of fibrous calcite cements that apparently replace foraminiferal tests. Journal of Sedimentary Petrology, 46: 545-547.

Kendall, A.C., 1985. Radiaxial fibrous calcite: a reappraisal. Schneidermann, N., Harris, P.M. (Eds), Carbonate Cements, 36. SEPM Special Publication: 59-77.

Kendall, A.C., Tucker, M.E., 1971. Radiaxial fibrous calcite as a replacement after syn-sedimentary cement. Nature-Physical Science, 232: 62-63.

Kendall, A.C., Tucker, M.E., 1973. Radiaxial fibrous calcite - replacement after acicular carbonate. Sedimentology, 20: 365-389.

Kim, S.-T., O'Neil, J.R., 1997. Equilibrium and nonequilibrium oxygen isotope effects in synthetic carbonates. Geochimica et Cosmochimica Acta, 61: 3461-3475.

Kim, Y., Lee, Y.I., 2003. Radiaxial fibrous calcites as low-magnesian calcite cement precipitated in a marine-meteoric mixing zone. Sedimentology, 50: 731-742.

Kluge, T., John, C.M., Jourdan, A.-L., Davis, S., Crawshaw, J., 2015. Laboratory calibration of the calcium carbonate clumped isotope thermometer in the 25–250° C temperature range. Geochimica et Cosmochimica Acta, 157: 213-227.

Lécuyer, C., Reynard, B., Grandjean, P., 2004. Rare earth element evolution of Phanerozoic seawater recorded in biogenic apatites. Chemical Geology, 204: 63-102.

Lees, A., Miller, J., 1995. Waulsortian banks. International Association of Sedimentologists SpecialPublication: Carbonate Mud-Mounds - Their Origin and Evolution, 23: 191-271.

Major, R., Wilber, R.J., 1991. Crystal habit, geochemistry, and cathodoluminescence of magnesian calcite marine cements from the lower slope of Little Bahama Bank. Geological Society of America Bulletin, 103: 461-471.

Mazzullo, S.J., 1980. Calcite pseudospar replacive of marine acicular aragonite, and implications for aragonite cement diagenesis. Journal of Sedimentary Petrology, 50: 409-422.

Mazzullo, S.J., Bischoff, W.D., Lobitzer, H., 1990. Diagenesis of radiaxial fibrous calcites in a subunconformity, shallow-burial setting - Upper Triassic and Liassic, Northern Calcareous Alps, Austria. Sedimentology, 37: 407-425.

Morford, J.L., Emerson, S., 1999. The geochemistry of redox sensitive trace metals in sediments. Geochimica et Cosmochimica Acta, 63: 1735-1750.

Neuser, R., Bruhn, F., Götze, J., Habermann, D., Richter, D., 1995. Kathodolumineszenz: Methodik und Anwendung. Zentralblatt für Geologie und Paläontologie Teil I, H, 1: 287-306.

Nozaki, Y., 2001. Rare Earth Elements and their Isotopes in the Ocean. Encyclopedia of Ocean Sciences, 4: 2354 - 2366.

Olivier, N., Boyet, M., 2006. Rare earth and trace elements of microbialites in Upper Jurassic coral- and sponge-microbialite reefs. Chemical Geology, 230: 105-123.

Passey, B.H., Henkes, G.A., 2012. Carbonate clumped isotope bond reordering and geospeedometry. Earth and Planetary Science Letters, 351–352: 223-236.

Pattan, J., Pearce, N., 2009. Bottom water oxygenation history in southeastern Arabian Sea during the past 140ka: Results from redox-sensitive elements. Palaeogeography, Palaeoclimatology, Palaeoecology, 280: 396-405.

Reeder, R.J., Grams, J.C., 1987. Sector zoning in calcite cement crystals: Implications for trace element distributions in carbonates. Geochimica et Cosmochimica Acta, 51: 187-194.

Richter, D., 1999. Hydra—Ein geologischer Überblick. Beiträge zur Sedimentologie von Griechenland.—Bochumer Geologische und Geotechnische Arbeiten53: 41-106.

Richter, D.K., Gotte, T., Niggemann, S., Wurth, G., 2004. REE3+ and Mn2+ activated cathodoluminescence in lateglacial and Holocene stalagmites of central Europe: evidence for climatic processes? Holocene, 14: 759-767.
Richter, D.K., Heinrich, F., Geske, A., Neuser, R.D., Gies, H., Immenhauser, A., 2014. First description of Phanerozoic radiaxial fibrous dolomite. Sedimentary Geology, 304: 1-10.
Richter, D.K., Immenhauser, A., Neuser, R.D., Mangini, A., 2015. Radiaxial-fibrous and fascicular-optic Mg-calcitic cave cements: a characterization using electron backscattered diffraction (EBSD). International Journal of Speleology, 44: 8.
Richter, D.K., Neuser, R.D., Schreuer, J., Gies, H., Immenhauser, A., 2011. Radiaxial-fibrous calcites: A new look at an old problem. Sedimentary Geology, 239: 23-36.
Richter, D.K., Riechelmann, D.F.C., 2008. Late Pleistocene cryogenic calcite spherolites from the Malachitdom Cave (NE Rhenish Slate Mountains, Germany): origin, unusual internal structure and stable C-O isotope composition. International Journal of Speleology, 37: 119-129.
Rimstidt, J.D., Balog, A., Webb, J., 1998. Distribution of trace elements between carbonate minerals and aqueous solutions. Geochimica et Cosmochimica Acta, 62: 1851-1863.
Römermann, H., 1969. Geologie der Insel Hydra (Griechenland). Philipps-Universität Marburg.
Saller, A.H., 1986. Radiaxial calcite in Lower Miocene strata, subsurface Enewetak-Atoll. Journal of Sedimentary Petrology, 56: 743-762.
Satterley, A.K., Marshall, J.D., Fairchild, I.J., 1994. Diagenesis of an Upper Triassic reef complex, Wilde-Kirche, Northern Calcareous Alps, Austria. Sedimentology, 41(5): 935-950.
Shenton, B.J., Grossman, E.L., Passey, B.H., Henkes, G.A., Becker, T.P., Laya, J.C., Perez-Huerta, A., Becker, S.P., Lawson, M., 2015. Clumped isotope thermometry in deeply buried sedimentary carbonates: The effects of bond reordering and recrystallization. Geological Society of America Bulletin: B31169. 1.
Shields, G.A., Webb, G.E., 2004. Has the REE composition of seawater changed over geological time? Chemical Geology, 204: 103-107.
Stolper, D.A., Eiler, J.M., 2015. The kinetics of solid-state isotope-exchange reactions for clumped isotopes: A study of inorganic calcites and apatites from natural and experimental samples. American Journal of Science, 315: 363-411.
Swart, P.K., 2015. The Geochemistry of Carbonate Diagenesis: The Past, Present and Future. Sedimentology, 62: 1233-1304
ten Have, T., Heijnen, W., 1985. Cathodoluminescence activation and zonation in carbonate rocks - an experimental approach. Geologie en Mijnbouw, 64: 297-310.
Thomson, J., Higgs, N.C., Wilson, T.R.S., Croudace, I.W., de Lange, G.J., van Santvoort, P.J.M., 1995. Redistribution and geochemical behaviour of redox-sensitive elements around S1, the most recent eastern Mediterranean sapropel. Geochimica et Cosmochimica Acta, 59: 3487-3501.
Tobin, K.J., Walker, K.R., Steinhauff, D.M., Mora, C.I., 1996. Fibrous calcite from the Ordovician of Tennessee: Preservation of marine oxygen isotopic composition and its implications. Sedimentology, 43: 235-251.
Tribovillard, N., Algeo, T.J., Lyons, T., Riboulleau, A., 2006. Trace metals as paleoredox and paleoproductivity proxies: an update. Chemical Geology, 232: 12-32.
van der Kooij, B., Immenhauser, A., Csoma, A., Bahamonde, J., Steuber, T., 2009. Spatial geochemistry of a Carboniferous platform-margin-to-basin transect: Balancing environmental and diagenetic factors. Sedimentary Geology, 219: 136-150.
van der Kooij, B., Immenhauser, A., Steuber, T., Bahamonde Rionda, J.R., Merino Tome, O., 2010. Controlling factors of volumetrically important marine carbonate cementation in deep slope settings. Sedimentology, 57: 1491-1525.
van der Kooij, B., Immenhauser, A., Steuber, T., Hagmaier, M., Bahamonde, J.R., Samankassou, E., Tome, O.M., 2007. Marine red staining of a Pennsylvanian carbonate slope: Environmental and oceanographic significance. Journal of Sedimentary Research, 77: 1026-1045.
Vaselli, L., Cortecci, G., Tonarini, S., Ottria, G., Mussi, M., 2012. Conditions for veining and origin of mineralizing fluids in the Alpi Apuane (NW Tuscany, Italy): Evidence from structural and

geochemical analyses on calcite veins hosted in Carrara marbles. Journal of Structural Geology, 44: 76-92.
Veizer, J., Ala, D., Azmy, K., Bruckschen, P., Buhl, D., Bruhn, F., Carden, G.A.F., Diener, A., Ebneth, S., Godderis, Y., Jasper, T., Korte, C., Pawellek, F., Podlaha, O.G., Strauss, H., 1999. Sr-87/Sr-86, delta C-13 and delta O-18 evolution of Phanerozoic seawater. Chemical Geology, 161: 59-88.
Wacker, U., Fiebig, J., Schoene, B.R., 2013. Clumped isotope analysis of carbonates: comparison of two different acid digestion techniques. Rapid Communications in Mass Spectrometry, 27: 1631-1642.
Watson, E.B., Baxter, E.F., 2007. Diffusion in solid-Earth systems. Earth and Planetary Science Letters, 253: 307-327.

Figure Captions

Fig. 1. Overview map of Europe with indication of sampled locations (red crosses) in Spain and Greece. Lower inset shows position of Hydra and Dokos (Greece).

Fig. 2. Photographs of hand specimens studied in the context of this paper. (A) Red-stained Bashkirian (Pennsylvanian) slope facies from the Sierra de Cuera platform, northern Spain. Note gray areas represent predominantly pores filled by radiaxial fibrous calcites or shell fragments. (B) Radiaxial fibrous calcite (dark gray) occluding cavities in Carnian to Norian (Upper Triassic) reefal limestone (light gray) from Hydra Island, Greece. (C) Cenomanian (Upper Cretaceous) radiaxial fibrous calcite (dark gray) occluding former pores between submarine breccia clasts (light gray) from Dokos Island, Greece.

Fig. 3. Main characteristic features of radiaxial fibrous (A) and fascicular optical fibrous (B) calcites. Modified after Richter et al. (2011). (SC = subcrystal; UCC = upward concave curvature of cleavage; DCC = downward concave curvature of cleavage; CWE = clockwise extinction; CCWE = counterclockwise extinction; MD = microdolomites; Z = cloudy zonation)

Fig. 4. Thin section photomicrographs of Upper Triassic radiaxial calcites documenting three characteristic types of cathodoluminescence properties found in all analyzed samples. Arrows indicate growth directions of crystals. (A/B) Upper Triassic radiaxial fibrous calcite under normal polarized light (A) and under luminescence (B; non- to intrinsic blue luminescence = n.l.). (C/D) Upper Triassic radiaxial calcite under normal polarized light (C) and showing patchy luminescence (D, p.l.). Boundaries between patchy

luminescent (p.l.) and non-luminescent (n.l.) portions of cements are well defined. (E) Polarized light photomicrographs of Upper Triassic radiaxial fibrous calcite fringes in hand specimen from Hydra Island (Fig. 2B). The image depicts central suture (S) of converging cement seams. (F) Image of same area under cathodoluminescence showing bright luminescence (b.l.).

Fig. 5. (A) Triassic hand specimen Rk-1-H. Black lines indicate boundary between sedimentary substratum (reefal limestone) and the cavity occluded by four subsequent generations of radiaxial fibrous calcites (RFC). Red dashed rectangle indicates position of the thin section shown in (C/D). (B) Cartoon illustrating position of two sampling transects (computer-controlled milling device used for sampling for isotope and ICP-MS analysis and LA-ICP-MS laser track, slightly below milled transect). (C) Photomicrograph of thin section mapped under crossed polarized light. Different generations of radiaxial fibrous calcite are labelled 1b/t through 4b/t. Cements precipitating on floor of cavity are indicated b (base), those growing from the ceiling of the pore towards the center of the pore are labelled t (top). Central suture is denoted as S. (D) Cathodoluminescence map of same area as C. White rectangle indicates position of the transect sampled for geochemical analyses (5B). White circles (C1-C4) denote sampling positions for clumped isotope measurements. White arrows indicate growth directions of cement paragenesis.

Fig. 6. Cross-plots of carbon and oxygen isotope data from all measured carbonate samples compared with reconstructed coeval seawater values from Veizer et al. (1999; green rectangles) and Bruckschen et al. (1999; black rectangle) and with carbon isotope values of marine calcite cements reported in Carpenter and Lohmann (1997, red dashed line). Note key to color code for non-, patchy and bright luminescent cements in lower right. (A) Isotope data from Bashkirian non-luminescent radiaxial calcites are enriched in ^{18}O relative to reconstructed seawater values whilst patchy and bright luminescent data plot within reconstructed marine range. (B) Data from Upper Triassic (Carnian/Norian) radiaxial calcites plot in narrow oxygen isotope range with luminescent sampling material being moderately depleted in ^{13}C

relative to non-luminescent ones. (C) Upper Cretaceous (Cenomanian) samples being enriched in ^{13}C relative to published values.

Fig. 7. Main and trace elemental concentrations of Carboniferous (Pennsylvanian; Bashkirian, Bashk.), Upper Triassic (Norian, Nor) and Upper Cretaceous (Cenomanian, Cen) radiaxial fibrous calcites plotted according to luminescence properties. Note generally lower elemental concentrations of Triassic and Cretaceous relative to Carboniferous cements. Decreasing Fe^{2+} and increasing Mn^{2+} concentrations as generally assigned to increasingly luminescent calcites are present in some cases (Pennsylvanian) but not obvious in Cretaceous and Triassic samples. Key for color coding is given in the lower right.

Fig. 8. Carbon and oxygen isotope as well as elemental abundances (lines show five-point moving average) plotted against the sampled transect in Upper Triassic radiaxial calcites (refer to Fig. 5 for location of sampled transect). Cathodoluminescence properties are shown to the left. Central suture is labelled S. Growth directions are indicated with arrows. Note symmetrical patterns in isotope ratios and elemental concentrations on both sides of central suture indicating that cements were not significantly overprinted.

Fig. 9. LA-ICP-MS data of Zn, Cd, U and Cu concentrations across transect in Upper Triassic case example. Lines show five-point moving averages. Symmetric patterns in Zn, Cd, Cu and U on both sides of the central suture (S) correlated to cement rims suggest absence of significant late stage overprint. Labels 1b/t through 4b/t correspond to the different cement phases (Figs 5 and 8). Central suture is labelled with S, growth direction indicated by arrows.

Fig. 10. Characteristic seawater REE patterns of the radiaxial fibrous calcite transect normalized to NASC (North American Shale Composite) values. Data are summarized for the different cement layers (1t/b through 4t/b) and labelled correspondingly. Ce concentrations are distinctly lower compared to the other REE (negative Ce-anomaly). One data point (layer 4t) shows positive Ce-anomaly. Thick lines indicate mean values of each cement layer.

Fig. 11. Ce/Ce* plot across sampled transect (cerium anomaly). Red line shows Lowess smoothing (10pts, α=0.1). Note significant Ce/Ce* peak at central suture indicating trend towards decreasingly marine and

increasingly suboxic conditions. This peak can be assigned to burial vein that crosscuts the transect. Central suture is indicated with S, growth directions are given as arrows.

Fig. **12.** Ce/Ce* vs. Pr/Pr* diagram (called La-anomaly) after Bau & Dulski (1996) to check for genuineness of Ce-anomalies. Data points that plot in field I show no anomaly. Data in field IIa shows positive La-anomaly which causes an apparent negative Ce-anomaly. IIb has positive La anomaly which leads to apparent positive Ce-anomaly. Data in field IIIa shows genuine positive Ce-anomaly. All data points that plot in field IIIb show a genuine negative Ce-anomaly. Data points are color coded regarding their assignment to the different cement layers.

Fig. 13. Paragenetic succession summarizing different depositional to diagenetic stages recorded in radiaxial fibrous calcites in sample Rk-1-H.

1056 Fig. 1

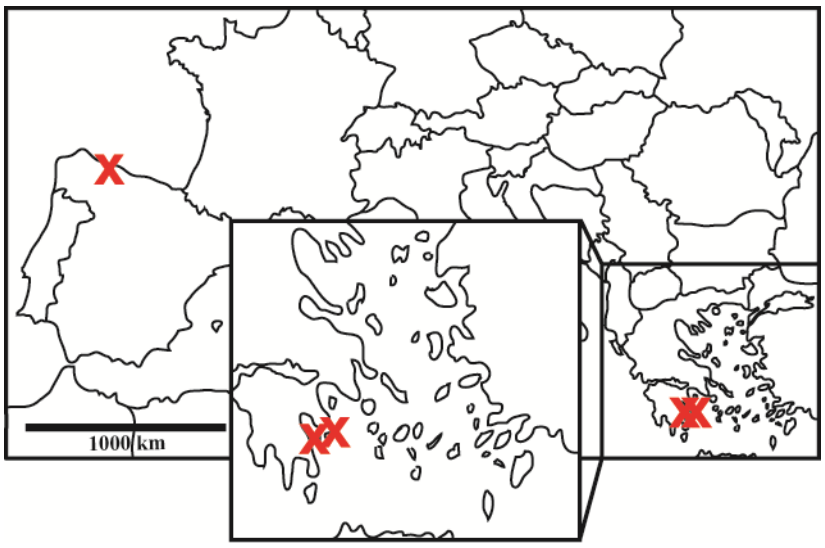

1057

1058

1059

1060 Fig. 2

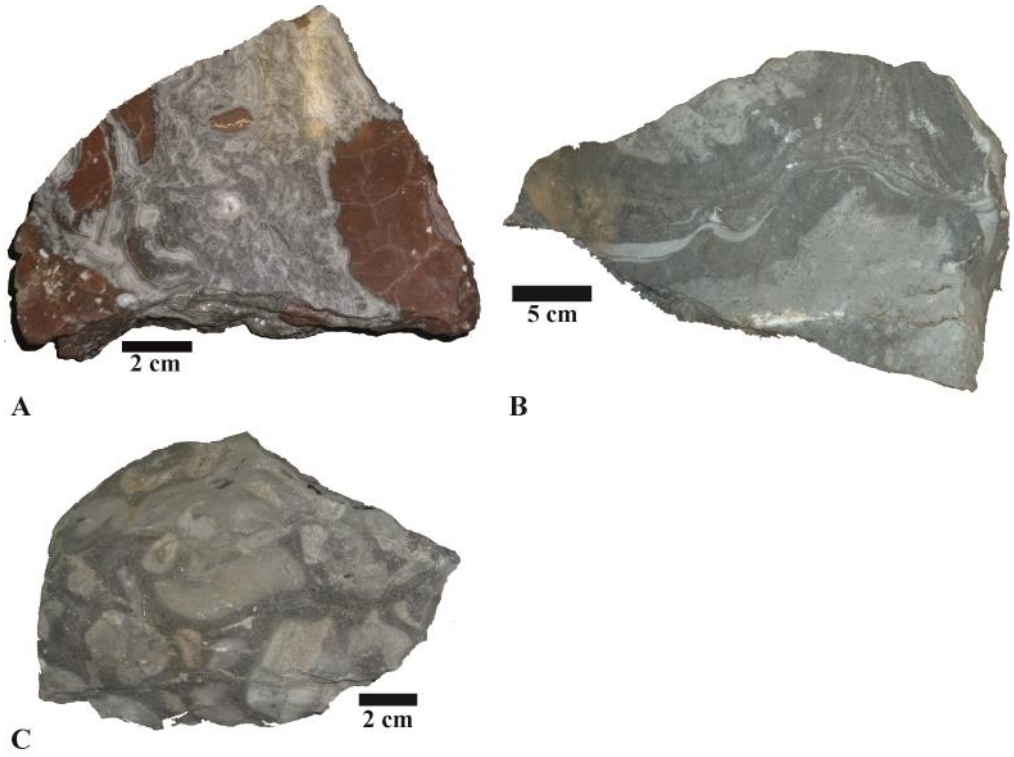

1061

1062

1063

1064 Fig. 3

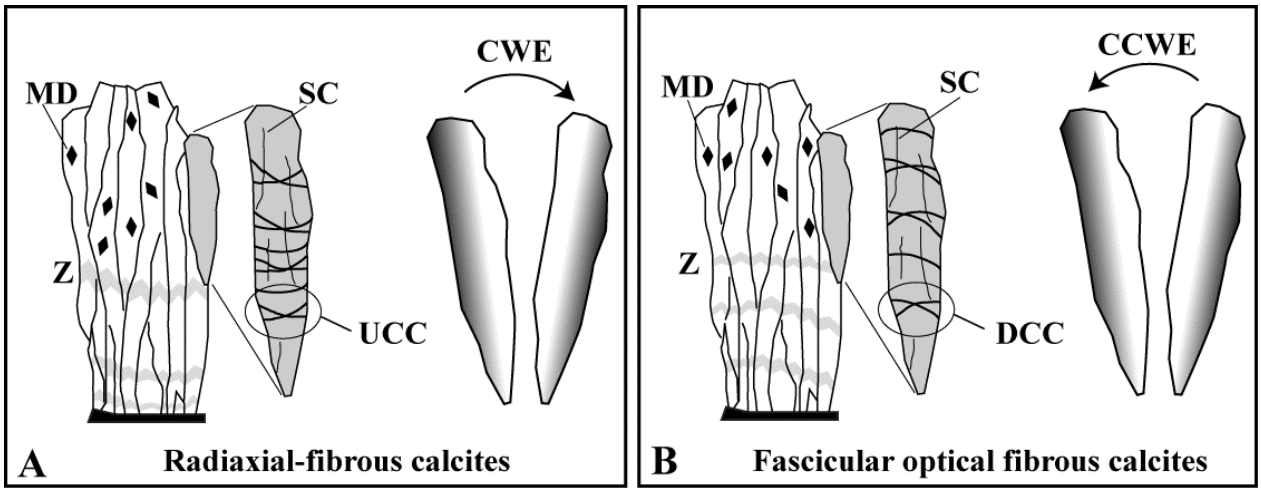

1065

1066

1067

1068 Fig. 4

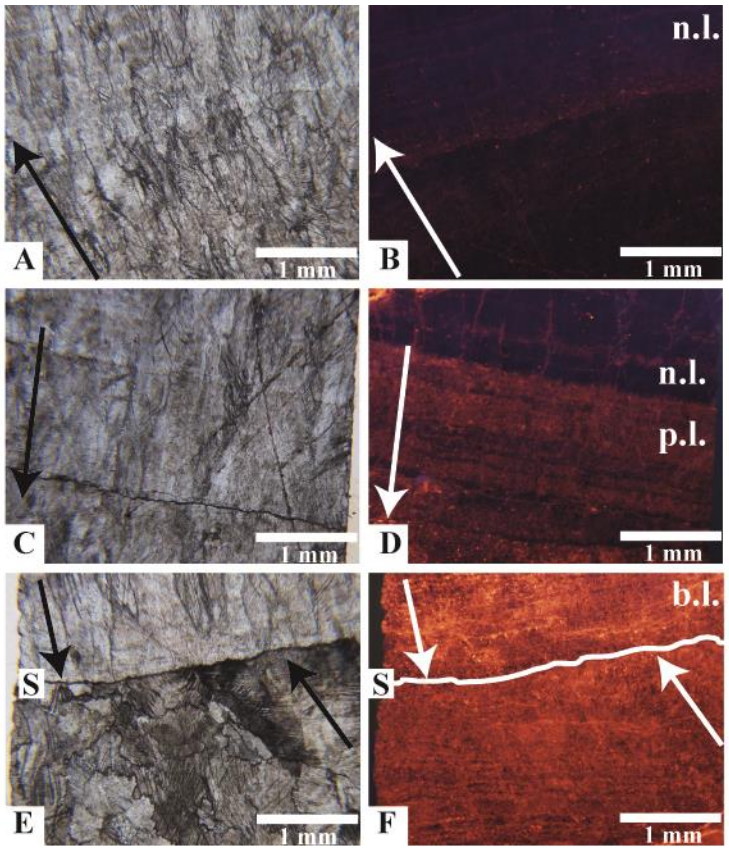

1069

1070

1071 Fig. 5

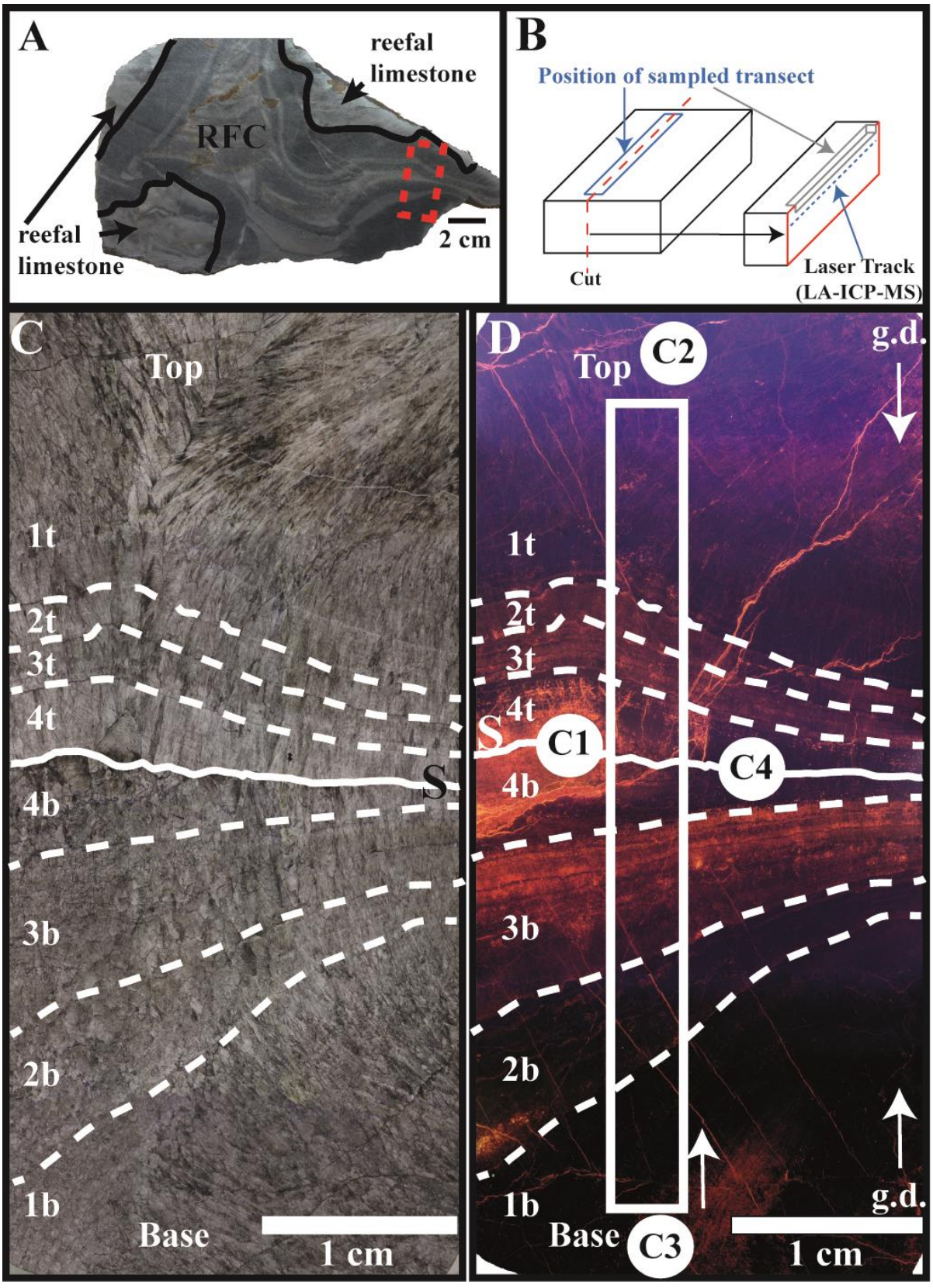

1072

1073 Fig. 6

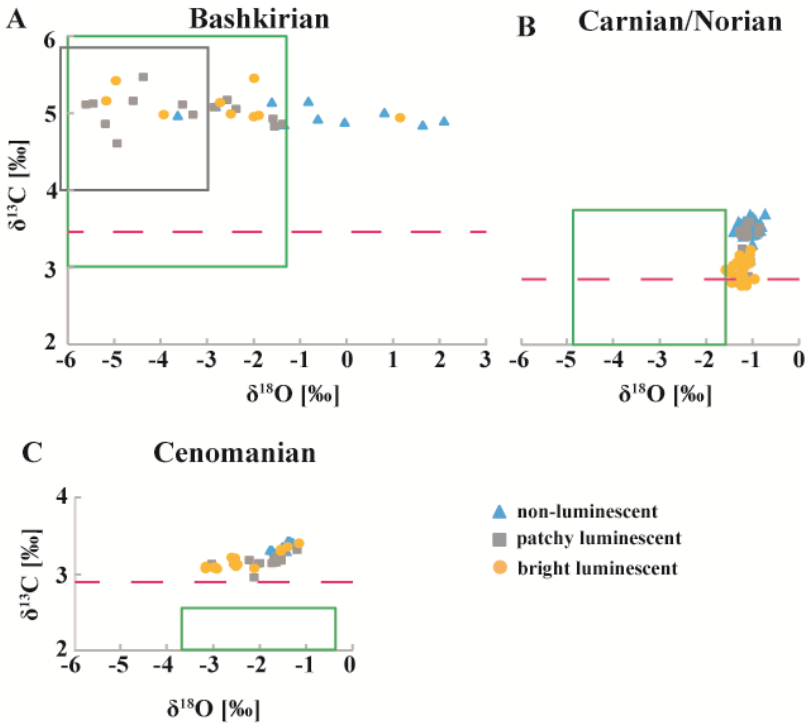

1074

1075 Fig. 7

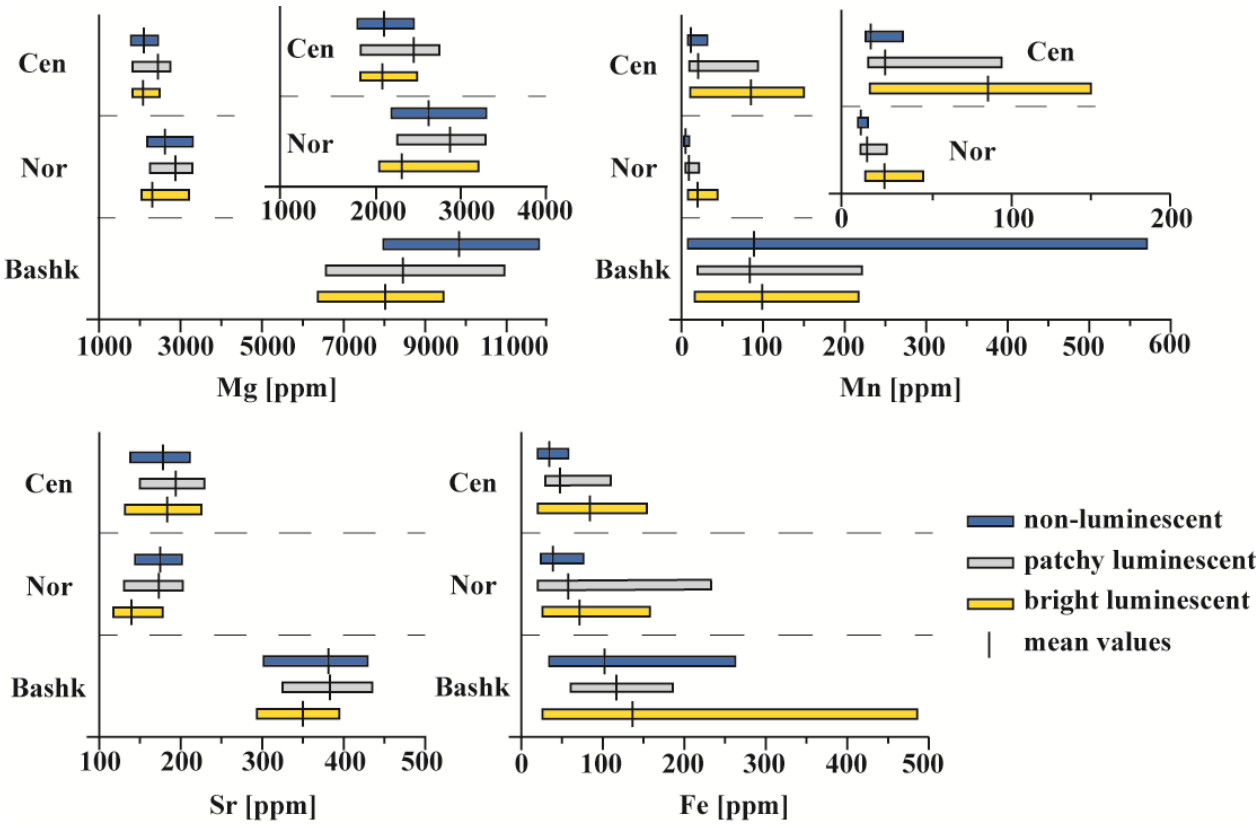

1076

Fig. 8

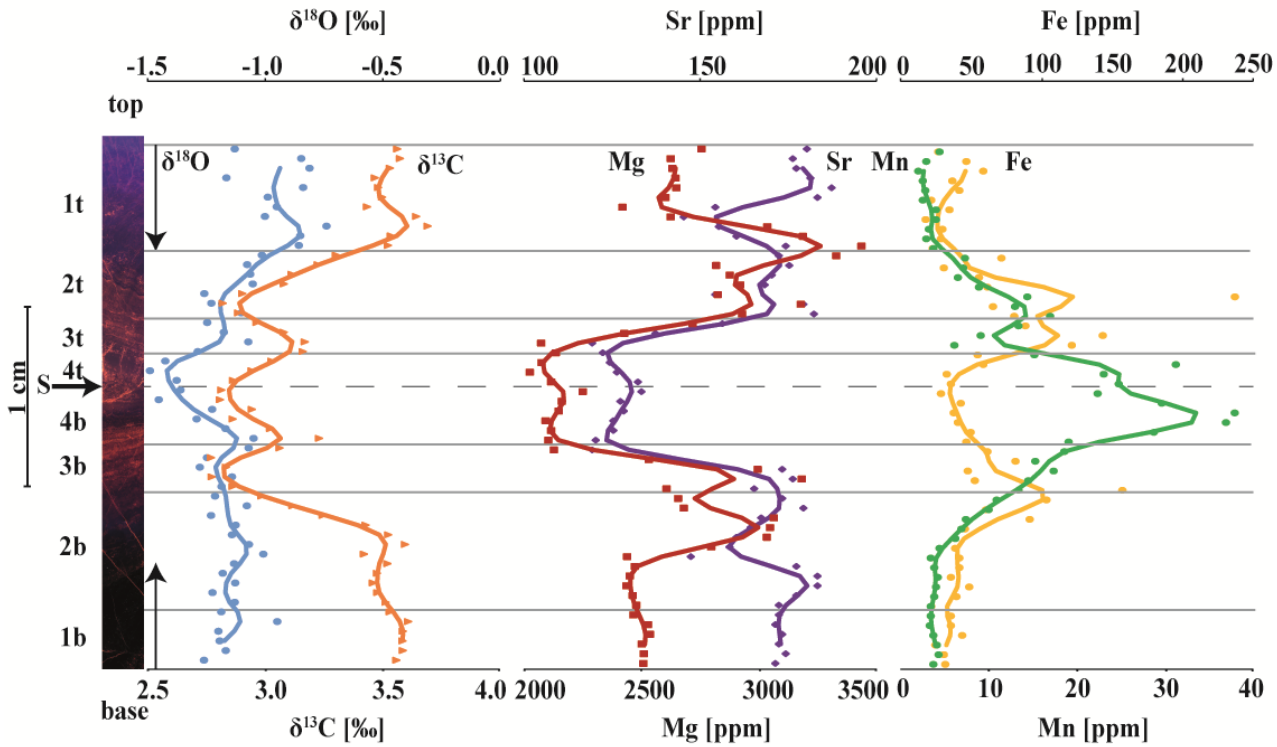
δ18O [‰]
-1.5
-1.0
-0.5
0.0
Sr [ppm]
100
150
200
Fe [ppm]
0
50
100
150
200
250
top
δ18O
δ13C
Mg
Sr
Mn
Fe
1t
2t
3t
4t
S
4b
3b
2b
1b
1 cm
base
2.5
3.0
3.5
4.0
δ13C [‰]
2000
2500
3000
3500
Mg [ppm]
0
10
20
30
40
Mn [ppm]

1092 Fig. 9

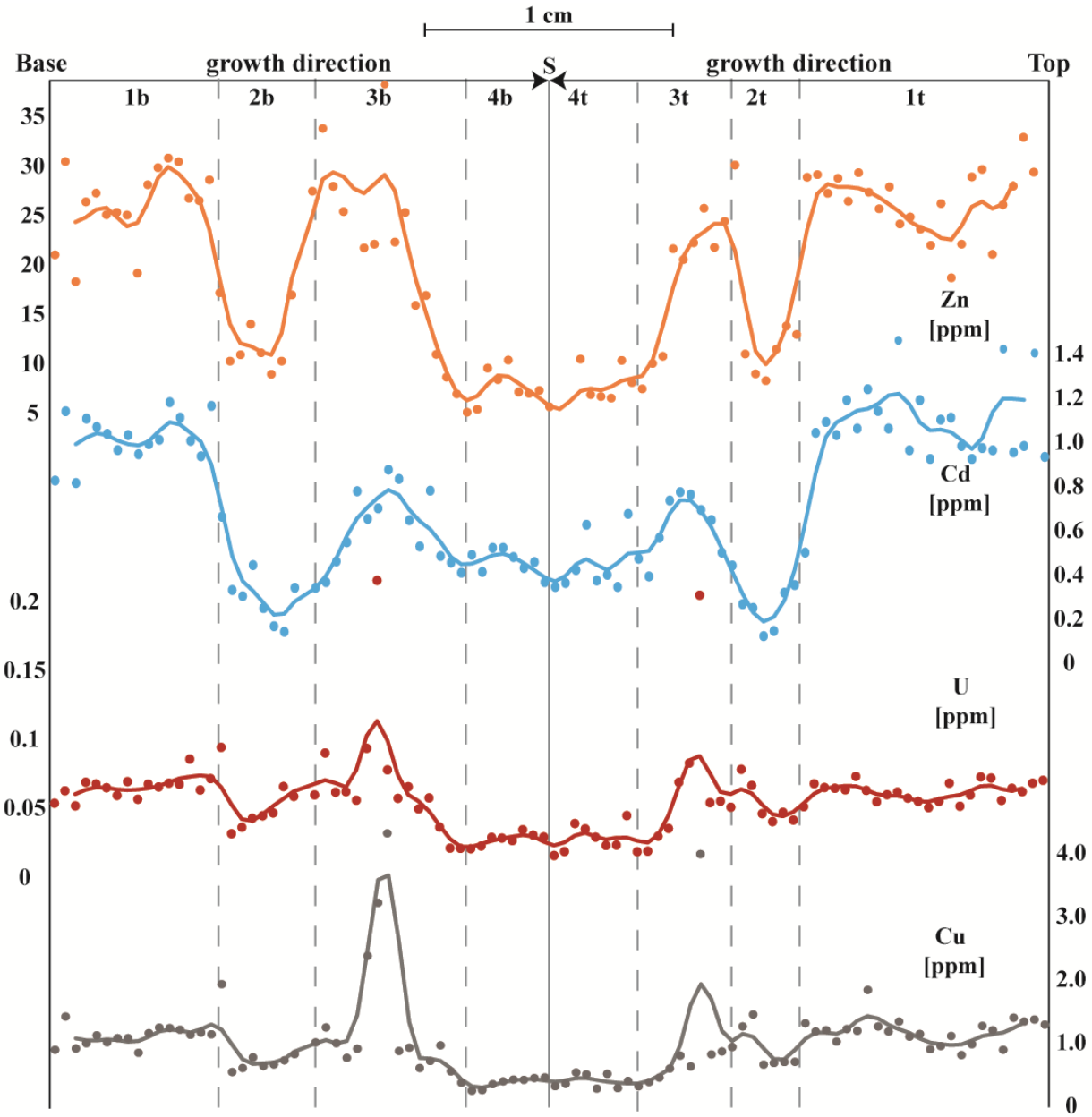

1093

1094

1095

1096

1097

1098

1099

1100 Fig. 10

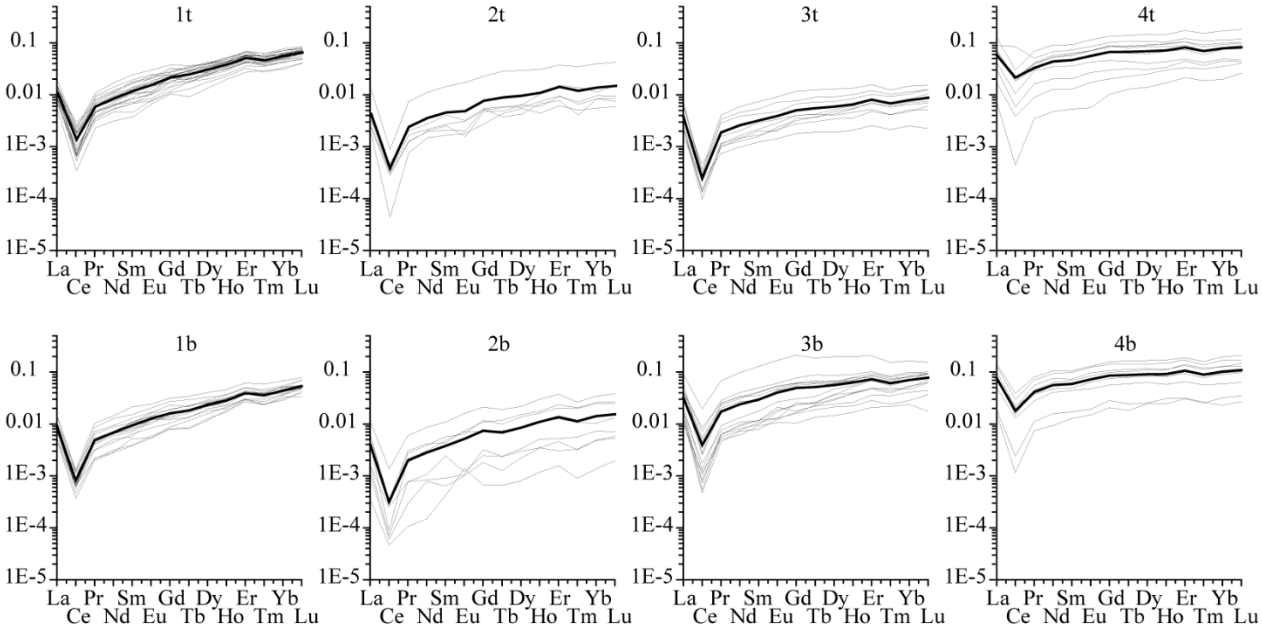

1101

1102

1103 Fig. 11

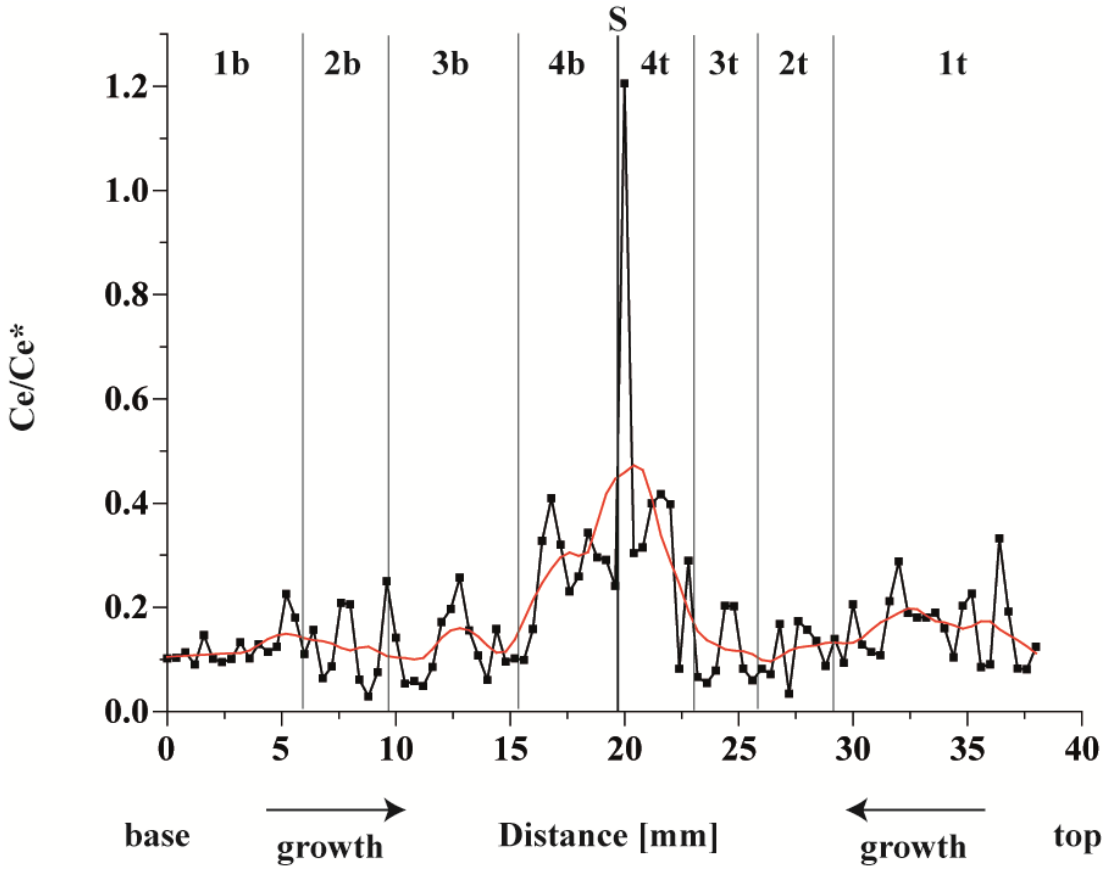

1117 Fig. 12

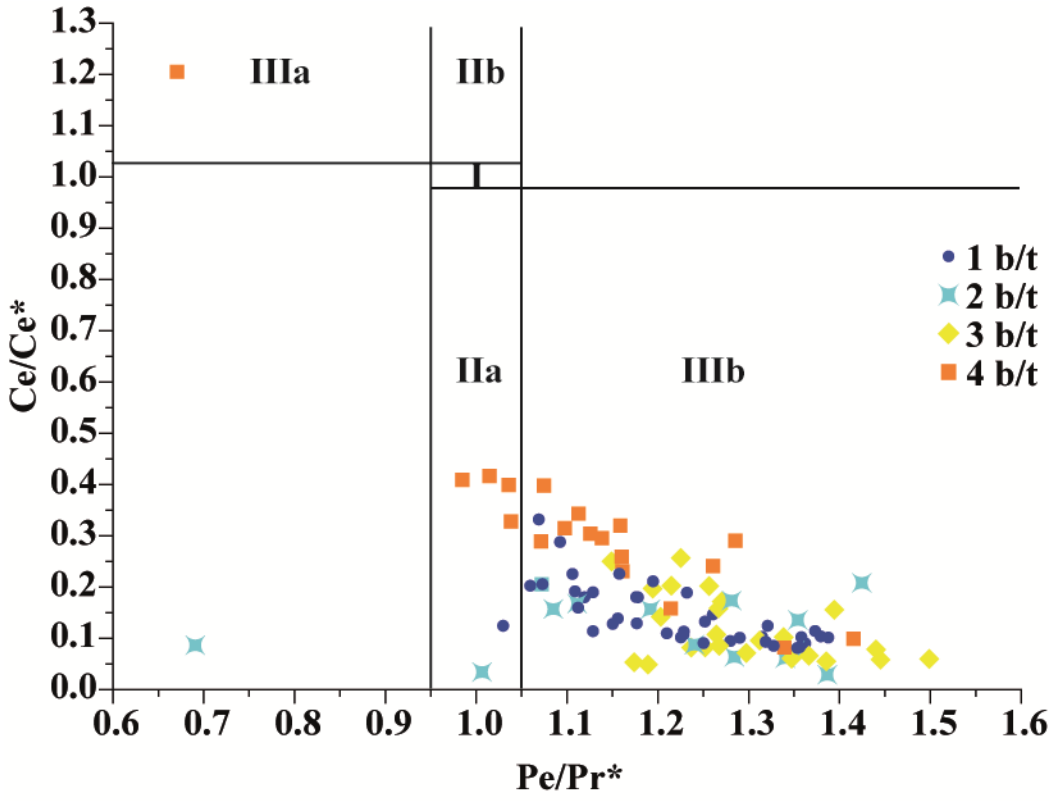

1118

1119 Fig. 13

1120

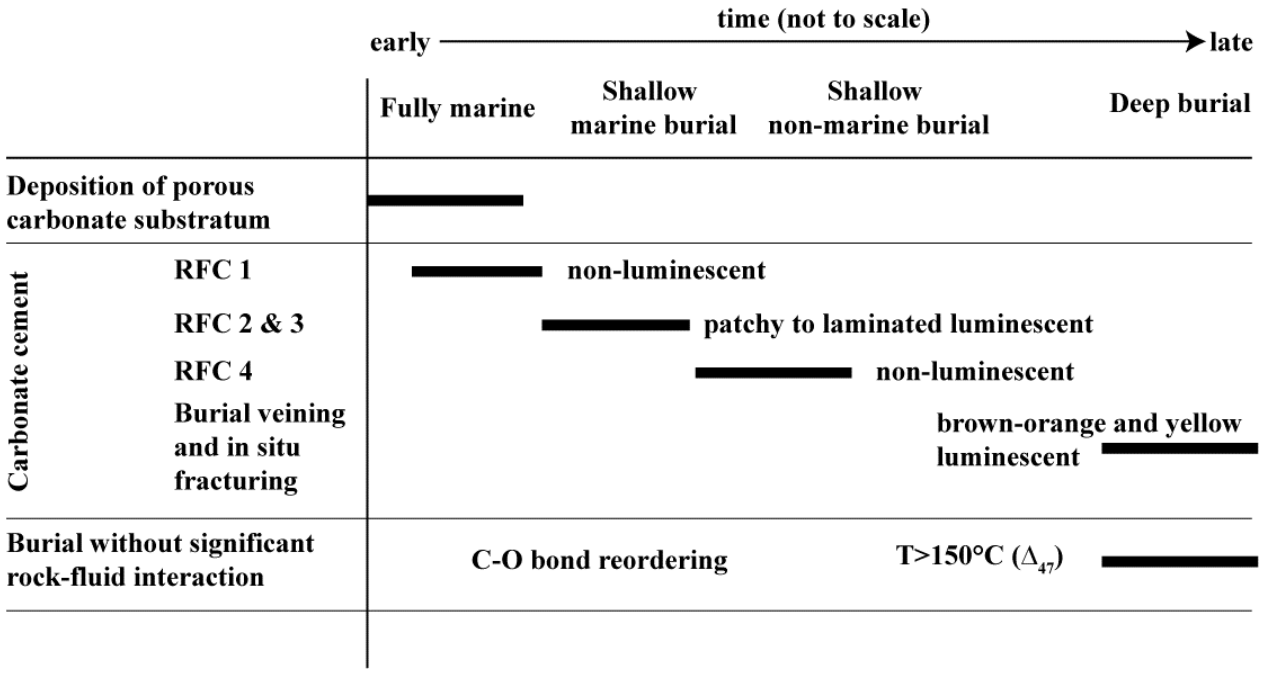

1121

Locality	Asturias (Spain)	Hydra (Greece)	Dokos (Greece)
Age	Late Carboniferous (Pennsylvanian (Bashkirian))	Late Triassic (Carnian)	Late Cretaceous (Cenomanian)
Carbonate platform type	High-rising platform (up to 850m), progradational geometry	Reef complex, progradational geometry	
Location on platform	Upper slope (150 - 350m below platform top)	Platform top, neritic	Platform top, neritic
Host facies	Red-stained microbial boundstone	Reefal limestone	Polymict limestone breccia
Sea-level-mode	Transgressive	Transgressive	Transgressive
Climate-mode	Icehouse	Greenhouse ("Hothouse")	Greenhouse
Global seawater chemistry	Aragonite-II sea	Aragonite-II sea	Calcite-II sea
	van der Kooij et al. (2007, 2009, 2010)	Richter (1999)	Bachmann and Riesch (1979), Clift & Robertson (1990)

Table 1. Description of the three different case settings analyzed in this study.

	luminescence pattern	δ13C [‰ V-PDB]			δ18O [‰ V-PDB]			Ca [ppm]			Mg [ppm]			Sr [ppm]			Fe [ppm]			Mn [ppm]			Ba [ppm]		
		Min	Max	Mean	Min	Max	Mean	Min	Max	Mean	Min	Max	Mean	Min	Max	Mean	Min	Max	Mean	Min	Max	Mean	Min	Max	Mean
Carboniferous	non-luminescent	4.8	5.2	5.0	-3.6	2.1	-0.7	379280	387230	384144	7482	11770	9901	302	430	382.2	32	266	103	5	571	88.1	0.8	2.3	1.3
Asturias	patchy luminescent	4.6	5.2	5.0	-3.6	2.1	-3.5	372580	389650	384629	6553	10930	8468	324	436	381.5	62	186	119.4	22.9	223	85.2	1.3	2.8	1.9
	bright luminescent	4.9	5.5	5.1	-5.2	1.1	-2.7	380960	390500	386582	6372	9473	8043	296	394	350.1	25	485	138.1	14.1	219	98.3	0.9	13.9	3.1
Triassic	non-luminescent	3.1	3.7	3.5	-1.4	-0.7	-1.1	386590	400210	394995	2397	3325	2616	145	203	175	17	71	38	1.9	7.2	3.9	0.8	1.7	1.4
Hydra	patchy luminescent	2.8	3.6	3.3	-1.4	-0.9	-1.2	386470	402620	394839	2245	3432	2830	133	205	171	22	237	59	3.6	22.3	9.3	0.9	2.1	1.3
	bright luminescent	2.8	3.2	3.0	-1.6	-1.0	-1.3	389270	403950	395305	2019	3178	2357	118	179	139	27	157	66	6	41.2	20.5	0.8	1.7	1.1
Cretaceous	non-luminescent	3.3	3.4	3.3	-1.8	-1.3	-1.5	382050	397430	394041	1779	2426	2159	138	209	177.6	20	54	33.8	5.5	28.9	10.9	1.3	7.2	2.1
Dokos	patchy luminescent	3.0	3.3	3.2	-3.0	-1.2	-1.9	388540	395520	390775	1847	2754	2435	149	230	193	28	109	47.7	7.1	90.4	20.8	1	2.4	1.9
	bright luminescent	3.1	3.4	3.2	-3.2	-1.2	-2.4	386190	396310	391763	1793	2508	2091	130	225	184.6	21	151	82.2	8.7	150	84.4	0.7	3.2	2.2

Table 2. Summary of isotope and trace elemental data.